

DOCTORAL DISSERTATION

---

# The Influence of Gravitationally Unstable Protoplanetary Disks on Type I Migration

(重力不安定原始惑星系円盤のI型惑星移動への影響)

---

*Author:*  
Ngan K. NGUYEN

*Supervisor:*  
Dr. Elizabeth J. TASKER

Graduate School of Science, Hokkaido University  
Department of Cosmoscience

September, 2020



## *Abstract*

The focus of this thesis is the impact of global structure in two types of astrophysical disks: galactic and protoplanetary.

The first chapter summarises a study on the impact of the global galactic environment on the physical properties of star-forming clouds. This work was the main focus of the Masters thesis and completed for the doctorate. A series of simulations of isolated galactic disks with varying background potentials were performed using an AMR hydrodynamics code. The galactic potentials are expressed by rising, decreasing and flat rotation curves, with the addition of either a massive stellar disk or two-armed spiral patterns. Results from these simulations explored the role of shear and the gravitational stability, Toomre  $Q$ , in the fragmentation of the gas disk into clouds. Although the properties of a typical cloud were found to be largely independent of the potential, the production of small and large cloud associations were strongly dependent on the galactic global structure. The addition of the spiral potential made the greatest difference to the clouds, successfully sweeping gas into extended structures.

In a similar system but on smaller scale, protoplanetary disks share an equivalent set of internal forces and an external global potential. The primary research for this thesis considers the instabilities forming in the protoplanetary disks that circle young stars and how this environment affects the evolution of planets forming from the dust and gas.

According to current theories, proto-planets are formed as a consequence of either a series of collisions and mergers between dust and solid material, or through a collapse from gravitational instabilities in the protoplanetary disk. However, the young planet is initially embedded within the protoplanetary disk and interacts with its parent gas disk through the exchange of angular momentum with the surrounding gas. This can cause the orbital radius of the planet to change, leading to a migration through the disk. Evidence for this phenomenon abounds in exoplanet systems, which have large planets on very short orbits that are unlikely to have formed in-situ.

Smaller planets undergo what is referred to as "Type I migration", which presents a major problem for planet formation theories. Numerical estimates of this process typically indicate a rapid inward migration, resulting in the loss of the planet. Young planets are sent into the star within approximately  $10^5$  years, from a distance of 1 AU, well before the protoplanetary disk can evaporate and remove the fatal gas pull from the planet (within  $10^6 - 10^7$  years).

In an attempt to prevent the loss of young planets, various possibilities have been discussed, including sharp changes in disk properties to create planet traps, late formation of planets after the disk has partially evaporated, and gravitational scattering by neighboring planets or planetesimals. However, recent ALMA observations have revealed complex substructures within the protoplanetary disks, including rings and spiral arms which could be results from either Lindblad waves ignited by planets or gravitational instability. Previous work has not typically focused on the effect of such structures formed by borderline stability of the protoplanetary disk on the migration of planets, typically assuming instead that the disk is homogeneous.

In this research, we perform a series of simulations of protoplanetary disks with different degrees of global structure and follow the migration of a young planet. The isolated protoplanetary disk is simulated using ChaNGa; an SPH hydrodynamics code. The disks exist in a variety of stable to borderline stable and unstable states, corresponding to different values of Toomre  $Q$ .

The planet's migration is strongly affected by instabilities that develop within the protoplanetary disk. While the planet's migration in a homogeneous disk moves inwards at a steady velocity, structure-rich disks disrupt this migration and cause an irregular motion through the gas. This is most clearly seen in the torques acting on the planet. These change from a settled constant value in a smooth gas distribution where resonance waves can be maintained, to experiencing strong fluctuations due to the formation of spirals and other features. Fragmentation of the disk can lead to scattering of the planet and ejection from the system. However, even disks with a Toomre  $Q > 1$  (representing stability) can still have a strong impact on the planet torques.

Overall, this work strongly suggests that massive or structure rich protoplanetary disks will also have an effect on the migration of the planet. This is expected for all protoplanetary disks in their early years and may apply to a wide variety of disks even at later times. Type I migration is therefore a highly non-linear process and can only be weakly approximated by an analytical expression in the majority of systems.



## *Acknowledgements*

I would like to express my deep gratitude to Dr. Elizabeth Tasker, my research supervisor for her kind support during past five years. Both of us are foreigners in Japan, but she has supported me as much as possible beside the role of an advisor, from the housing when I moved to Tokyo for the first time to the accommodations when we went abroad. It was a tough beginning to switch from familiar galaxies to new protoplanetary disks, however, this was a chance for me to learn a lot from my supervisor how to tackle an unfamiliar problem. This thesis cannot be completed without her patient guidance and enthusiastic encouragement. I wish I could be as optimistic and energetic as her. Moreover, the result is not only the thesis, but also my skills (like programming, writing, searching, planning) have gradually been improved during doing PhD, especially presenting skill, as I really enjoyed Elizabeth's talks, which were logically coherent science stories (even though I need much more attempt).

I would like to offer my special thanks to Professor James Wadsley at McMaster University for his valuable suggestion in code development in this research work. We had many insightful discussions via emails and during the short time in Hamilton, Canada.

My thanks are also extended to the technicians of Cray XC50 systems at the Center for Computational Astrophysics (CfCA) of the National Astronomical Observatory of Japan (NAOJ) and JAXA supercomputer system (JSS) on which our numerical computations were conducted successfully.

Assistance provided by members of Astrophysics lab and the Office for International Academic Support at Hokkaido University, and Users Office at Institute of Space and Astronaut Science (ISAS/JAXA) was greatly appreciated, as various paperwork needs their help to be translated and completed.

I also greatly appreciate my parents, who let me go abroad and believe I can survive and succeed. I know your feeling and worry are typical of Asian parents, but I did my best to overcome your concern and proved that I can live independently far from you thanks to your love and care. Special thanks to my husband, Anh D. Phan, who always encourages me to do what I desired. Despite the distant love and marriage (even when we were in the same country), he is a great supporter and has unconditionally loved me (by saying that a lot). Not only a soul-mate enjoying relaxing time

with me, is he a role model for a true scientist for me to imitate. I truly thank him for sticking by my side during my good and bad times.

Last but not least, I wish to thank my friends for providing support and friendship when we were far from hometown.

# Contents

<b>Abstract</b>	<b>iii</b>
<b>Acknowledgements</b>	<b>v</b>
<b>Contents</b>	<b>vii</b>
<b>List of Figures</b>	<b>ix</b>
<b>1 From Galactic Disk to Protoplanetary Disk</b>	<b>1</b>
<b>2 Type I Migration and Challenges</b>	<b>7</b>
2.1 Torque of gas disk on a planet . . . . .	9
2.2 Type I migration and the challenge for forming planets . . . . .	11
<b>3 Numerical Methods and Early Simulations</b>	<b>15</b>
3.1 ChaNGa - a smoothed particle hydrodynamics code . . . . .	15
3.2 Initial conditions . . . . .	16
3.2.1 Surface density . . . . .	16
3.2.2 Temperature of the disk . . . . .	17
3.2.3 Star and Planet . . . . .	18
3.2.4 Adjustments to the code for this project . . . . .	18
The temperature floor . . . . .	18
Planet growth . . . . .	19
3.3 Initial runs . . . . .	19
3.3.1 Effect of cooling rate on disk stability . . . . .	19
3.3.2 Migration in an unstable disk . . . . .	23
<b>4 Simulating Disk Instability with Migration</b>	<b>25</b>
4.1 First simulation results . . . . .	25
4.2 Matching Type I migration . . . . .	34
4.2.1 Low-mass planet in a homogeneous light disk . . . . .	34
4.2.2 Resolution sensitivity of migration . . . . .	42
4.3 Type I migration in borderline unstable disks . . . . .	45
4.3.1 A massive planet in a heavy disk . . . . .	45
4.3.2 A low-mass planet in a heavy disk . . . . .	49

4.4 Conclusion . . . . . 52

# List of Figures

1.1	The structure of each gas disk after $t = 300$ Myr of evolution. Projections show a $32 \times 32$ kpc region and show the gas surface density integrated vertically over $ z  \leq 1$ kpc. Each column shows the different type of rotation curve (denoted by the last character: rising R, decreasing D and flat F) and each row shows a different model type (Fiducial Fi, Extreme Ex, Stellar Disk St, Spiral Sp). The gas disks are fully fragmented into clouds in most of models at all radii except for the ER (i.e. Extreme Rise) model. . . . .	2
1.2	The Toomre- $Q$ parameter in the gas for all simulations in this study as a function of radius (at $t = 300$ Myr). The horizontal dashed line shows the 2D stability limit of $Q = 1$ and the horizontal solid line the approximate 3D stability limit of $Q = 0.67$ (Kennicutt, 1998). . . . .	3
1.3	The shear parameter, $S$ , in the gas for all simulations in this study as a function of radius (at $t = 300$ Myr). The shear stability limit of $S = 1$ . is shown by the solid horizontal line. . . . .	4
1.4	Cloud mass distribution in comparisons of the fiducial models (dashed line) and the other ones (solid line). Typical cloud mass is roughly $10^{5.5} M_{\odot}$ . . . . .	5
2.1	High angular resolution continuum observations of planet forming disks obtained with ALMA. From left to right and from top to bottom: TW Hya, V883 Ori, HD 163296, HL Tau, Elias 2-27, and HD 142527. Credits: S. Andrews, L. Cieza, A. Isella, A. Kataoka, B. Saxton (NRAO/AUI/NSF), and ALMA (ESO/NAOJ/NRAO). . . . .	8
2.2	The gas close to planet moves in horse shoe orbit indicated by solid blue line. . . . .	9
3.1	Distribution of surface density of 4 disks, in which from left to right, top to bottom, the instability of the disk is expected to increase, corresponding to cooling parameter $\beta_{\text{cool}} = 20, 13, 11.5,$ and $10$ . The red dot indicates the planet location. . . . .	21

3.2	Toomre $Q$ , surface density and temperature profiles of various protoplanetary discs (top to bottom). In the top plot, horizontal dotted line indicates the critical value of stability and the vertical dashed line estimates the position of the planet at the beginning. In the middle plot, the dotted line presents the MMSN surface density. . . . .	22
3.3	The variation of planet orbital radius in protoplanetary disks. The straight lines in matching colour present theoretical estimation of type I migration timescale. . . . .	24
4.1	Toomre $Q$ , surface density and temperature profiles of the three protoplanetary discs in Table 4.1 (top to bottom). In the top plot, the horizontal dotted line indicates the critical value of stability and the vertical dashed line estimates the position of the planet at the beginning of the simulation. In the bottom plot, the dashed line indicates the location of the cooling floor. . . . .	26
4.2	The 2D distribution of surface density of various disks at different stability degrees and red dot indicates the planet's location. From left to right, the disk are respectively <b>Stable</b> light disk, <b>semi-stable</b> light disk, <b>Semi-stable Heavy</b> disk. The red dot indicates the planet location in the disk. . . . .	28
4.3	The variation of planet orbital radius in the protoplanetary disks. Solid line indicates the analytical expectation of the migration based on Eq. 2.9	29
4.4	The 2D distribution of torque around planet. From left to right, the disk are respectively Stable light disk, Semi-stable light disk, Semi-stable Heavy disk . . . . .	30
4.5	The net torque (excluding Roche sphere) averaged over 1 orbit then normalized by $-10^{29} \text{kgm}^2\text{s}^{-2}$ . . . . .	30
4.6	The net torque (excluding Roche sphere) averaged over 1 orbit then normalized by $\tau_{avg}$ calculated over first 15 orbits after planet's development completes. . . . .	31
4.7	The net torque (excluding Roche sphere) averaged over 20 orbits in comparison with linear estimation (dashed lines in matching colors) taken from Tanaka, Takeuchi & Ward (2002). . . . .	33
4.8	Top to bottom: Radial distribution of the gravitational instability parameter (Toomre $Q$ ), surface density and temperature of the disk with mass of $0.005 M_{\odot}$ . Black dashed lines indicate disk profiles before inserting planet but after the disk settled. The vertical lines in middle panel indicate locations of the planet (solid) and the innermost/outermost Lindblad resonances (dashed left/right) at the last output, i.e. 1248 years. Green dashed curve in bottom panel denotes the minimum temperature. The Toomre $Q$ (top) is always above 1. . . . .	35

4.9	The 2D distribution of surface density of the light disk ( $0.005 M_{\odot}$ ) after planets $10 M_{\oplus}$ (top) and $33 M_{\oplus}$ (bottom) finish their growth. . . . .	37
4.10	The orbital variation of two planets in protoplanetary disk of mass $0.005 M_{\odot}$ . The dashed lines in matching colors indicate the growth in mass of the planets. . . . .	38
4.11	The evolution of the gas torque on $10 M_{\oplus}$ planet in $0.005 M_{\odot}$ disk. The linear estimation (black solid line) and numerical fitting (black dashed line) are taken from Tanaka, Takeuchi & Ward (2002) and D'Angelo & Lubow (2010), in comparison with averaged torque excluding the vicinity around planet (within 0.5, 1 and 1.5 Hill radius). The lower panel is for comparison at the same scale with Fig. 4.12 and 4.22 . . . . .	39
4.12	Same as Figure 4.11, but for $33 M_{\oplus}$ planet in $0.005 M_{\odot}$ disk. . . . .	40
4.13	The orbital evolution of a $10 M_{\oplus}$ planet in $0.005 M_{\odot}$ disk resolved by two resolutions: 1 million (thick lower line) and 2 million (thin upper line) particles. The red line indicates the growth in mass of the planet. . . . .	43
4.14	The evolution of averaged torque exerted on $10 M_{\oplus}$ planet by $0.005 M_{\odot}$ disk resolved by two resolutions: 1 million (thick lines) and 2 million (thin lines) particles. . . . .	44
4.15	Top to bottom: Radial distribution of instability parameter, surface density and temperature of the massive disk ( $0.07 M_{\odot}$ ). The black dashed lines indicate disk profiles before inserting planet. The horizontal line in top panel illustrated $Q = 1$ . The vertical lines in middle panel indicate locations of the planet (solid) and the innermost/outermost Lindblad resonances (dashed left/right) at the last output, i.e. 1165 years. The green dashed curve in bottom panel denotes the minimum temperature. . . . .	46
4.16	The 2D distribution of surface density of the massive disk ( $0.07 M_{\odot}$ ) after the planet (denoted by the green dot) finishes its growth. . . . .	47
4.17	The variation of planet orbital radius in protoplanetary disk of mass $0.07 M_{\odot}$ (black line). The red line indicates the increase in mass of the planet. . . . .	48
4.18	The evolution of the gas torque on $33 M_{\oplus}$ planet in $0.07 M_{\odot}$ disk. Same denotation as in Figure 4.11 . . . . .	50
4.19	Same as Figure 4.15 for a $10 M_{\oplus}$ planet in a massive disk of $0.0875 M_{\odot}$ , $T = 250 KR^{-1}$ . . . . .	51
4.20	The 2D distribution of surface density of the massive disk ( $0.0875 M_{\odot}$ ) after $10 M_{\oplus}$ planet finishes its growth. . . . .	53
4.21	The variation of planet orbital radius in protoplanetary disk of mass $0.0875 M_{\odot}$ (black line). The red line indicates the growth in mass of the planet. . . . .	54

4.22 Same as Figure 4.11, but for  $10 M_{\oplus}$  planet in  $0.0875 M_{\odot}$  disk. The lower panel is in same scale as that in Figure 4.11, 4.12 for comparison. . . . . 55



## Chapter 1

# From Galactic Disk to Protoplanetary Disk

The initial months of the doctorate thesis focused on investigating how star-forming giant molecular clouds are influenced by different galactic environments. This research was the primary focus during the Masters thesis, and the work was accepted for publication in the Monthly Notices of the Royal Astronomical Society (MNRAS) in December 2017 (Nguyen, et al., 2018). This chapter presents a brief summary of this topic.

Giant molecular clouds are composed of cold, dense gas and are formed during the gravitational collapse of gas when self-gravity reigns over other resistant factors, including thermal pressure and rotational support. The empirical relation between the surface density of the star formation rate and that of the gas reveals a surprising dependence of sub-parsec scale phenomena on kilo-parsec regions (Schmidt, 1959; Kennicutt, 1998). Observation of a more efficient star-forming process in starburst galaxies is evidence for this sensitivity to the global galactic-scale (Daddi et al., 2010).

One explanation for this empirical result is that the properties of the giant molecular clouds are sensitive to the galactic global structure, providing different environments that impact the resulting star formation rate. Differences in cloud properties between the extreme outer edge and the inner regions of our Galaxy (Roman-Duval et al., 2010; Izumi et al., 2014; Sun et al., 2017), or within the spiral and inter-arm regions of galaxy M51 (Koda et al., 2009; Meidt et al., 2012), support the idea that the local environment is having an important role on the cloud formation. Inspired by these apparent dependencies, we utilised an AMR hydrodynamics code, ENZO, to simulate isolated galaxies in various background potentials (Brummel-Smith, et al., 2019).

Four different sets of background potentials were considered: **Fiducial** from a general galactic disk with a rotation velocity of about  $200 \text{ km s}^{-1}$ , similar to that expected for the Milky Way, **Extreme** where the maximum circular velocity was dramatically increased up to  $500 \text{ km s}^{-1}$ , **Stellar Disk** where the gas disk density followed the stellar

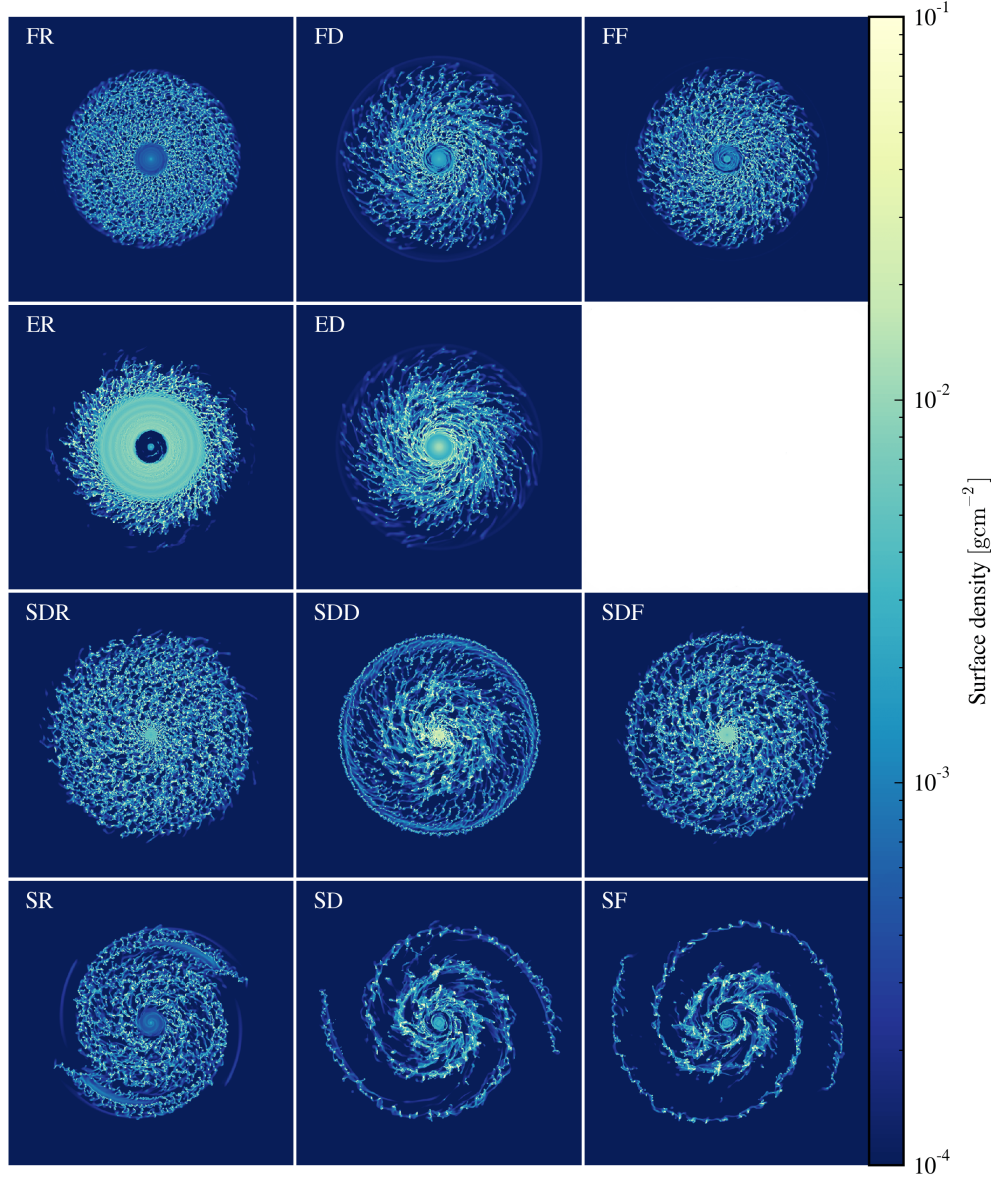


FIGURE 1.1: The structure of each gas disk after  $t = 300$  Myr of evolution. Projections show a  $32 \times 32$  kpc region and show the gas surface density integrated vertically over  $|z| \leq 1$  kpc. Each column shows the different type of rotation curve (denoted by the last character: rising R, decreasing D and flat F) and each row shows a different model type (Fiducial Fi, Extreme Ex, Stellar Disk St, Spiral Sp). The gas disks are fully fragmented into clouds in most of models at all radii except for the ER (i.e. Extreme Rise) model.

profile to create a more realistic galaxy at the cost of varying the properties of the gas disk between runs, and **Spiral** which included an additional two-arm spiral potential. Each potential set included three rotation curves (except for **Extreme**, which just used

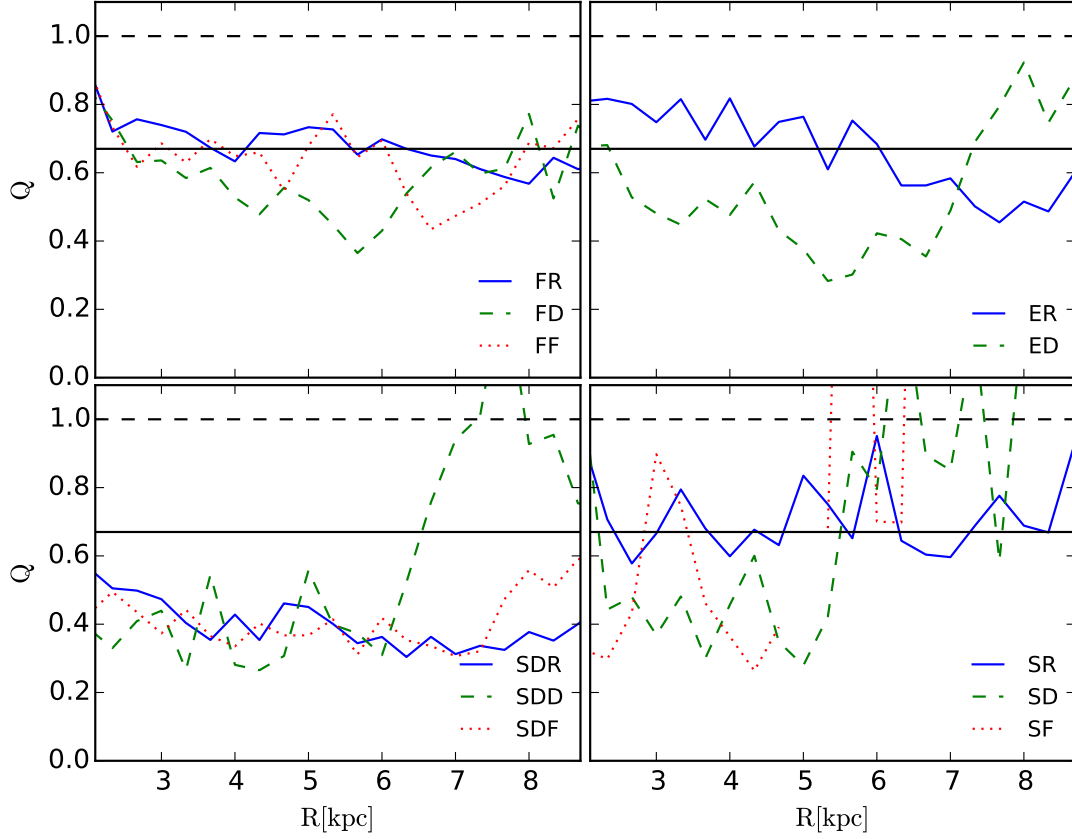


FIGURE 1.2: The Toomre- $Q$  parameter in the gas for all simulations in this study as a function of radius (at  $t = 300$  Myr). The horizontal dashed line shows the 2D stability limit of  $Q = 1$  and the horizontal solid line the approximate 3D stability limit of  $Q = 0.67$  (Kennicutt, 1998).

two), consisting of *Rising*, *Falling* and *Flat*. These are predicted from halo dominated, disk dominated and Milky Way-like galaxies, respectively.

The evolution of these disks resulted in different fragmentation structures, corresponding to different stability determined by gravitational collapse (Toomre  $Q$ ) and shear (see Figure 1.1). Here, the Toomre  $Q$  and shear parameter  $S$  are defined as:

$$Q = \frac{\kappa c_s}{\pi G \Sigma_g} \quad (1.1)$$

$$S = \frac{2.5 \sigma_g A}{\pi G \Sigma_g} \quad (1.2)$$

where  $A$  is an Oort constant,  $c_s$ ,  $\Sigma_g$ ,  $\kappa$  are gas sound speed, surface density, and epicycle frequency, respectively. The structure in the disk begins developing when  $Q < 1$  (in 3D case,  $Q < 0.67$ ) and  $S < 1$  (Toomre, 1964; Dib et al., 2012).

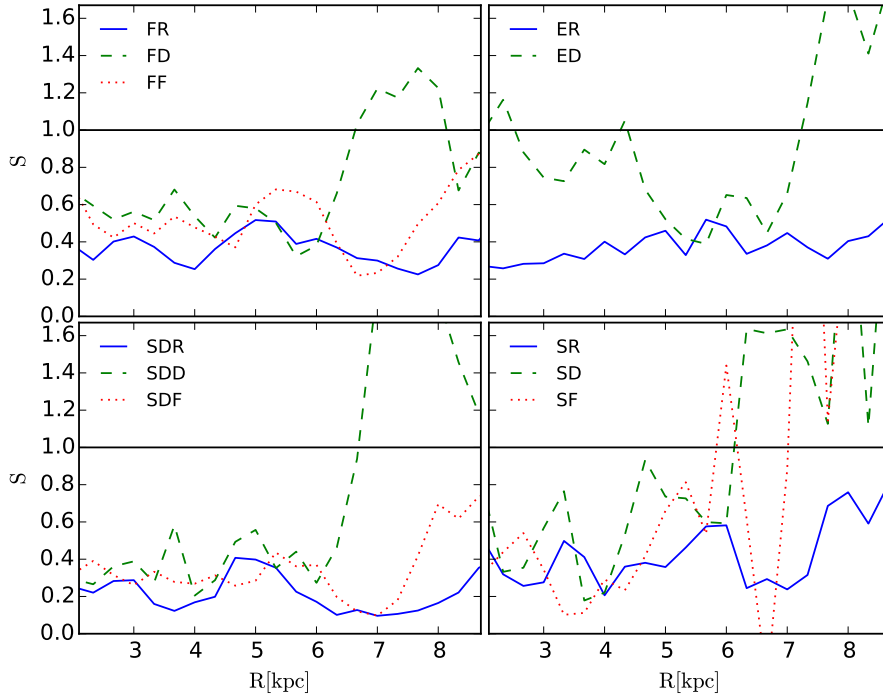


FIGURE 1.3: The shear parameter,  $S$ , in the gas for all simulations in this study as a function of radius (at  $t = 300$  Myr). The shear stability limit of  $S = 1$ , is shown by the solid horizontal line.

The factor driving stability is revealed in the **Extreme** runs. In the Extreme Rising simulation, the resistance to collapse in the inner region is a consequence of the high epicycle frequency raising  $Q$  (Figure 1.2), allowing the low shear rate to prevail. Contrary to this, in the outer edges of the Extreme Decreasing disk, shear throttles collapse to prevent the fragmentation (Figure 1.3). Linked with this, the potential environment also determined the response of the disk to an applied spiral perturbation. Disks with rising velocity curves correspond to dark matter dominated disks whose mass overrules the spiral model excitation in the lighter stellar disk.

Although the sensitivity of disk structure on the global environment influences where clouds originally form, the properties of a typical cloud were unaffected by the changes in rotation curve. Here, clouds are identified if gas density is over  $n_{\text{thresh}} \geq 100 \text{ cm}^{-3}$ . However, the small and large cloud associations show the great variation in their physical properties, relevant to the stability of the gas disk. Figure 1.4 shows one of cloud properties we explored, cloud mass distribution in comparisons of the fiducial models (dashed line) and the other ones (solid line). The **Extreme** rotation curves with either greater gravitational stability or more shear support produced a tail of larger clouds. Similarly, the addition of spiral in **Spiral** runs and the utility of massive gas disk in **Stellar Disk** set also lead to the enhancement in both cloud size and cloud number density. In general, lower levels of shear across the galactic disk such as those in the **Rise** curves of all sets produced a uniform fragmentation that led cloud profiles

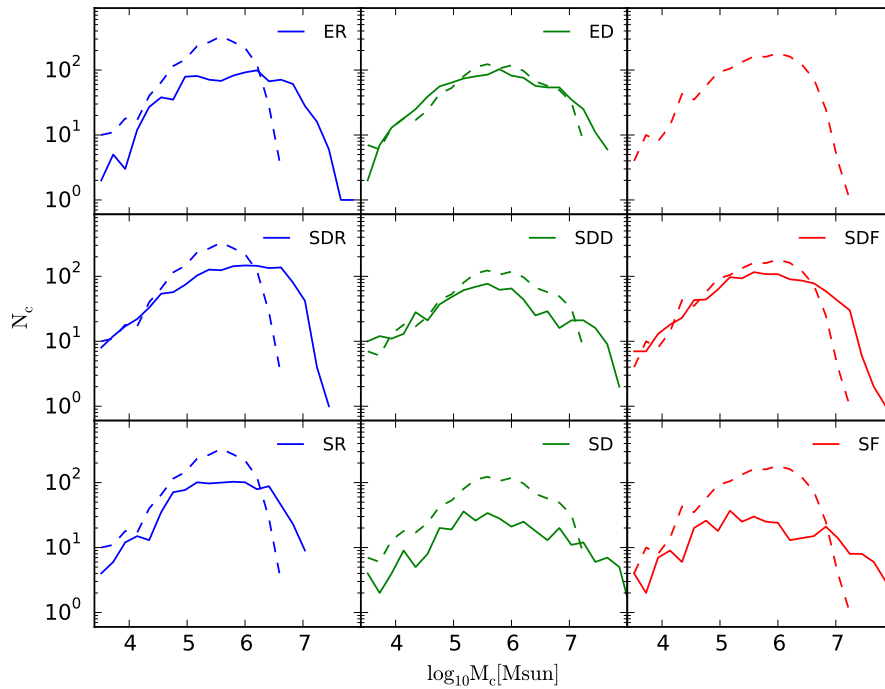


FIGURE 1.4: Cloud mass distribution in comparisons of the fiducial models (dashed line) and the other ones (solid line). Typical cloud mass is roughly  $10^{5.5} M_{\odot}$ .

concentrated around the peak values, with smaller tails. Overall, the strongest impact on the cloud population was made by the inclusion of the spiral potential. This swept cloud gas into the spiral arms, producing GMA (Giant Molecular Associations)-sized structures with broader profile of properties than for the flocculent runs.

During the formation of the star within cores of gas within the giant molecular clouds, the gas falls into a rotating disk surrounding the central star due to the conservation of angular momentum. This is called the protoplanetary disk. While on a much smaller scale than the galactic disks considered here (galaxy disks are 10s of kiloparsecs across, while protoplanetary disks extend to 10s of AU: 1 AU is  $4.8 \times 10^{-9}$  kpc), the system shares similarities. As with the galactic disk, protoplanetary disks experiences internal forces such as gravity and thermal pressure, and external forces from the global potential. Soon after its formation, the disk is relatively massive and becomes vulnerable to gravitational instabilities and other external factors. This can lead to a more perceptible disk structure owing to the excitation of density wave spirals. [Pérez, et al. \(2016\)](#) observed distinct spiral patterns in a protoplanetary disk for the first time but the cause of it is still in discussion.

While the work in this chapter looked at the effect on stars born in different structures of galactic discs, the rest of this thesis will look at the effect on a proto-planet born into different structures of protoplanetary disk.



## Chapter 2

# Type I Migration and Challenges

Current theories of planet formation are divided into two main approaches: core accretion and disk instability. A planet formed via the core accretion process is the result of a chain of collisions and accumulations of dust grains and variously sized solid components. The second scenario of disk instability is similar to star formation, in which the early massive protoplanetary disk fragments into clumps to form giant planet cores with gaseous envelopes. Whichever method forms the planet, the young world exists within- and interacts with- its parent gaseous disk.

The exact size of a protoplanetary disk remains a subject of speculation. A minimum disk can be found for our own Solar System by considering the mass of the planets smeared out into annuli about their orbital position, with elements added to match the solar elemental abundances. This gives the Minimum Mass Solar Nebula or MMSN, and represents the minimum amount of material needed to build the eight planets orbiting our Sun, assuming no material is lost. The total mass is approximately  $0.01 M_{\odot}$  and the surface density profile is typically given by (Hayashi, 1981):

$$\Sigma = 150 \left( \frac{r}{5 \text{ AU}} \right)^{-3/2} \text{ g cm}^{-2} \quad (2.1)$$

In practice, the initial mass of our protoplanetary disk was certainly significantly higher. Protoplanetary disks are known to have viscosity, leading to an accretion onto the central star. Additionally, material is lost from the disk during photoevaporation, and even entire planets may be lost after formation in gravitational encounters between neighbouring worlds.

Further evidence for significantly heavier protoplanetary disks has come from observations of extrasolar systems. While many of the discovered exoplanets are considered to have formed within a protoplanetary disk of mass 1 – 3% of the stellar mass, others have been discovered that require a mass of order ten times higher (Morales, et al., 2019; Haworth, et al., 2018).

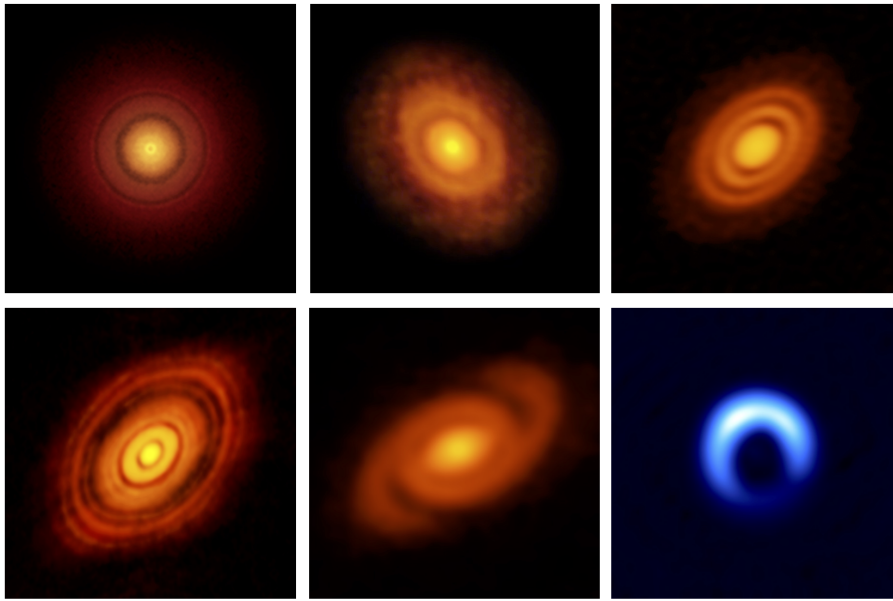


FIGURE 2.1: High angular resolution continuum observations of planet forming disks obtained with ALMA. From left to right and from top to bottom: TW Hya, V883 Ori, HD 163296, HL Tau, Elias 2-27, and HD 142527. Credits: S. Andrews, L. Cieza, A. Isella, A. Kataoka, B. Saxton (NRAO/AUI/NSF), and ALMA (ESO/NAOJ/NRAO).

The earlier stage in the planet formation process has been imaged using the Atacama Large Millimeter/submillimeter Array (ALMA) to observe the dust in protoplanetary disks around young stars. These images (Figure 2.1) show clear structure in these disks, which may be the result of planet formation but may also be driven by gravitational instabilities in the disks themselves, suggesting a dense profile (Dong, Najita & Brittain, 2018).

Even for a lightest MMSN-sized protoplanetary disk, the interaction between the disk and the growing planet is a key part in the evolution of the planetary system. Initially, the solid material in the protoplanetary disk is suspended in the gas and moves at the same velocity. However, as the planet grows, it decouples from the gas to move at the slightly-slower Keplerian velocity. By the time the planetary embryo has grown to the size of Mars (approximately 10% of an Earth mass), its gravitational pull has a strong effect on the parent gas disk. The disk-planet interaction is described simply by the so-called impulse approximation in which the planet's gravity pulls on the gas and the gas pulls back. The consequence is an exchange of angular momentum and the planet's orbit is influenced. This is known as "migration". Migration comes into two different types: low mass planets migrate in so called "Type 1 migration", while massive planets open a physical gap at their orbital position within the protoplanetary disk and move at a different rate known as "Type 2 migration".

Although there is no direct observational evidence for gas disk driven migration,



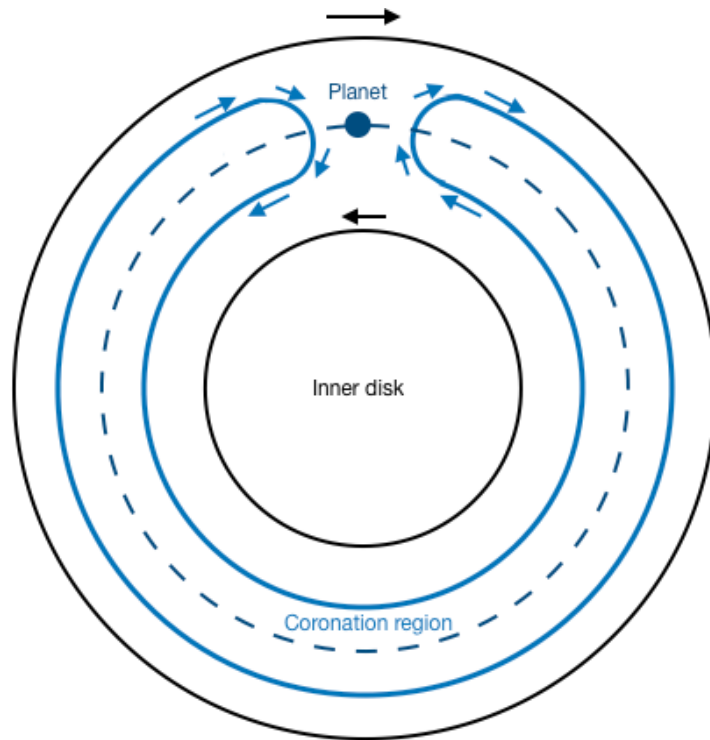


FIGURE 2.2: The gas close to planet moves in horse shoe orbit indicated by solid blue line.

the discovery of Hot Jupiter is believed a consequence of this mechanism (Mayor & Queloz, 1995). Such a giant exoplanet with Jovian mass is expected to be born in the region external to ice line, where temperature is low enough for abundant icy materials to exist, but it orbits very close to the host star. A possible explanation for this is that the planet interacts with the gas disk, and drifts from its original location to current position.

## 2.1 Torque of gas disk on a planet

Strong interaction between the planet and protoplanetary disk occurs due to the creation of disk resonances. Resonance exists when a gas disk exchanges angular momentum with the planet within it. The total torque of the gas disk on the planet generally composes of corotation torque and Lindblad torque. Assuming the planet orbits a central star of mass  $M_s$  on a circular orbit with radius  $R_p$ , it has Keplerian angular velocity,  $\Omega_p = \sqrt{GM_s/R_p^3}$ . Resonance occurs when:

$$m(\Omega - \Omega_p) = \pm\kappa \quad (2.2)$$

where  $m$  is an integer, and  $\kappa$ , the epicyclic frequency, is defined as  $\kappa = \left(\frac{d^2\Phi_0}{dR^2} + 3\Omega^2\right)$  with  $\Phi_0$  is the stellar potential. In case of Keplerian disk,  $\kappa = \Omega$ .

The first case,  $m = 0$ , i.e.  $\Omega = \Omega_p$ , refers to corotation resonance, which arises at radius in the disk where gas corotates with the planet. In case of low-mass planet, applying linear theory for corotation resonance estimates a positive torque, which impedes the differential Lindblad torque to slow down inward migration (Nelson, 2018). Generally, however, the linear corotation torque is not large enough to significantly restrain the rapid inward migration.

In non-linear theory, the gas is actually not at the same orbital radius with the planet, but moves in a horseshoe orbit relative to planet position (see Figure 2.2). When changing from the exterior orbit to interior orbit, i.e. from low density to high density regions, and vice versa, the gas fluid elements exchange angular momentum with the planet at the U-shaped turns. More work on horseshoe drag showed the non-linear corotation torque depends strongly on vorticity and entropy gradient in the disk (Paardekooper & Mellema, 2006; Masset & Casoli, 2010). If the viscosity of the disk is sufficiently large, the corotation torque remains its significant impact on the evolution of planet motion, in forms of either linear or non-linear expressions depending on planet-to-star mass ratio. Corotation torque, by contrast, vanishes in a disk of very low viscosity, called corotation saturation, leaving only Lindblad torque control the migration of the planet (Paardekooper & Papaloizou, 2009).

Non-zero  $m$  corresponds to inner (+) and outer (−) Lindblad resonances. These resonances locate where density waves are excited by an embedded planet in a gas disk. When the planet interacts with gas disk inside its orbit, it gains angular momentum from the gas disk and tends to migrate outward. On the contrary, interaction with gas disk exterior to the orbit makes the planet lose angular momentum and move toward the central star. The outer Lindblad resonances are slightly closer to the planet than the inner, so the total Lindblad torque is normally dominated by the outer torque, resulting in inward migration of the planet. Positions of Lindblad resonances are determined by:

$$R_L = \left(1 \pm \frac{1}{m}\right)^{2/3} R_p \quad (2.3)$$

where  $R_p$  is the planet orbital radius. The outermost Lindblad resonance  $m = 1$  occurs where  $\Omega = \Omega_p/2$  and innermost  $m = 2$  where  $\Omega = 2\Omega_p$ . Nonetheless, the inclusion of disk self-gravity and gas pressure causes an inward shift of both inner and outer Lindblad resonances (Baruteau & Masset, 2008a; Papaloizou, et al., 2007). When  $m \rightarrow \infty$ , the resonances get very close to the planet orbit, and interior to  $R_L = R_p \pm 2H/3$ , they contribute little to the net torque (Goldreich & Tremaine, 1980; Artymowicz, 1993). Here  $H$  is the pressure scale height of the disk, defined as:

$$H = \frac{c_s}{\Omega} \quad (2.4)$$

with  $c_s$  and  $\Omega$  are sound speed and circular velocity of the disk.

Total torque on planet is then a summation of Lindblad and corotation torques:

$$T_{net} = \sum T_L + T_{CR} \quad (2.5)$$

## 2.2 Type I migration and the challenge for forming planets

A low-mass planet normally induces small perturbations in a light homogeneous gas disk, so it does not affect the disk structure significantly. Hence, the torque on planet can be obtained using linear analysis.

Throughout this thesis, we focus on a planet of low mass  $M_p$  locating at orbital radius  $R_p$  in a gaseous disk with surface density  $\Sigma$  and temperature  $T$  in form of radial power-law:  $\Sigma \propto R^{-\alpha}$ ,  $T \propto R^{-\beta}$ . If the planet receives a net torque presented in equation 2.5, it will migrate at the rate of:

$$\frac{dR_p}{dt} = 2 \frac{T_{net}}{M_p} \sqrt{\frac{R_p}{GM_s}} \quad (2.6)$$

In attempt to figure out the net torque on planet, [Ward \(1997\)](#) and [Tanaka, Takeuchi & Ward \(2002\)](#) applied linear analytical calculations to a fully isothermal disk (i.e.  $T = \text{constant}$ ;  $\beta = 0$ ). They obtained the following expressions for the differential Lindblad and corotation torques acting on the planet:

$$T_{L,lin} = -(2.34 - 0.1\alpha)\Gamma_0; \quad T_{CR,lin} = (0.976 - 0.641\alpha)\Gamma_0 \quad (2.7)$$

Here, the torque is normalized by:

$$\Gamma_0 = \left( \frac{M_p R_p \Omega_p}{M_s c_s} \right)^2 \Sigma_p R_p^4 \Omega_p^2 \quad (2.8)$$

where  $\Sigma_p, c_s$  denote surface density and sound speed evaluated at location of the planet, respectively.

Hence, the net torque of a homogeneous fully isothermal 3D disk on the planet is determined by:

$$T_{lin} = -(1.364 + 0.541\alpha)\Gamma_0 \quad (2.9)$$

As a result from Eq. 2.6, the time-scale for inward migration is given by:

$$\tau = (2.7 + 1.1\alpha)^{-1} \frac{M_s}{M_p} \frac{M_s}{\Sigma_p R_p^2} \left( \frac{c_s}{R_p \Omega_p} \right)^2 \Omega_p^{-1} \quad (2.10)$$

In a MMSN protoplanetary disk with  $\Sigma = 150(r/5AU)^{-3/2}$  g cm<sup>-2</sup> and a temperature at 5 AU of  $T = 130$  K, an Earth-mass planet forming at 5 AU is sent into the Sun within

approximately  $\tau = 8 \times 10^5$  year. This inward migration time scale is much shorter than the expected lifetime of the disk, which is expected to be around  $10^6 - 10^7$  years before the gas and remaining dust are dispersed through accretion or photoevaporation. This theoretical calculation of the torque and resultant timescales agrees with results from numerical simulations performed by [D'Angelo, Kley & Henning \(2003\)](#); [Bate, et al. \(2003\)](#).

This equation can be modified by considering a locally isothermal disk (i.e. radially varying temperature,  $\beta \neq 0$ ) with softened gravity included to account for 3D effect. The resultant non-linear net torque is calculated by [Paardekooper, et al. \(2010\)](#):

$$T_{nl, P} = \left[ -(2.5 - 0.1\alpha - 0.5\beta) \left( \frac{0.4}{b/h} \right)^{0.71} - 1.4\beta \left( \frac{0.4}{b/h} \right)^{1.26} + 1.1 \left( \frac{3}{2} - \alpha \right) \left( \frac{0.4}{b/h} \right) \right] \Gamma_0 \quad (2.11)$$

where  $b$  is the softening parameter and  $h$  is the disk aspect ratio. The last two terms in the square bracket indicate the non-linear horseshoe corotation torque. A further improved formula for torque was developed by [D'Angelo & Lubow \(2010\)](#) using 3D numerical simulations on a disk with radially varying temperature to adjust the constant:

$$T_{nl, D} = -(1.36 + 0.62\alpha + 0.43\beta)\Gamma_0 \quad (2.12)$$

where  $\Gamma_0$  is defined in Eq. 2.8.

As all of these approximations resulted in the rapid loss of the forming planet, a range of numerical simulations have been attempted to stop this fast inward movement using more realistic disks. These included [Jang-Condell & Sasselov \(2005\)](#) who added cooling processes and found unperturbed non-isothermal disk and planet-induced temperature perturbations could reduce migration rate of the planet. [Ayliffe & Bate \(2010\)](#) discovered a light (MMSN-like) grain opacity disk might reduce the rate of low mass planet migration. [Menou & Goodman \(2004\)](#) concluded impact of different background disks (mass accretion, viscosity parameter) on planet migration. A diminished migration rate is expected in adiabatic disks ([Baruteau & Masset, 2008b](#)) and with an addition of magnetic field ([Nelson & Papaloizou, 2004](#); [Guilet, Baruteau & Papaloizou, 2013](#)).

Recently, outward migration also is favored in either radiative diffusion disk ([Lega, et al., 2014](#)) or considering thermal torque due to planet's accretion ([Guilera, et al., 2019](#)). [Paardekooper & Mellema \(2006, 2008\)](#) used fixed rotating coordinate frames of a low mass disk (as MMSN) to show an outward migration in high opacity inner region, agreeing with [Kley & Crida \(2008\)](#) and [Kley, Bitsch & Klahr \(2009\)](#).

Planet traps have also been considered as a solution, allowing the planet to be temporarily held on a given orbit due to transitions within the disk in heat, density, opacity or turbulence that can produce a zero-torque region where direction of the planetary migration may change from inward to outward. This possibility could halt the rapid fall toward the star (e.g. Hasegawa & Pudritz (2011); Lyra, Paardekooper & Mac Low (2010); Bitsch & Kley (2011); Baillié, Charnoz & Pantin (2016)).

Despite this myriad of ideas, no convincing solution to the migration problem has been acquired. The solution needs to be one that still permits migration –as many exoplanets are found on short orbits where it would be difficult to accumulate sufficient solid material to form in-situ– but in the vast majority of cases allows planets to survive, suggesting that the necessary disk conditions cannot be rare.

A less explored solution is that the migration of the planet is strongly affected by the structure of the disk. As highlighted at the start of this chapter, recent ALMA and SPHERE observations with sufficient resolution reveal complex substructures within protoplanetary disks, including spiral arms which could be results from either Lindblad waves ignited by planets or gravitational instability (e.g. Christiaens, et al. (2014); Pérez, et al. (2016); Stolker, et al. (2016); Boehler, et al. (2018); Andrews, et al. (2018)), rings and gaps claiming the existence of planets (e.g. Fedele, et al. (2017, 2018)). Several images of protoplanetary disks obtained with ALMA are shown in Figure 2.1.

In the extreme case of gravitational instability, planets can form through disk instabilities as an alternative to the core accretion formation model as proposed by Boss (1989). But, more recent simulations show that protoplanetary disks are usually stable within about 40 AU (Rogers & Wadsley, 2012). This suggests that planet formation is more likely to take place via core accretion. But does that mean the observed disk structure is entirely unimportant? Or can it still affect planet formation and resultant system architecture by changing the fate of a migrating planet?

Previous works mentioned above have not typically focused on this borderline stability case, assuming the disk is homogeneous. Baruteau & Masset (2008a) considered a self-gravitating disk to find an inverse relation between Toomre  $Q$  (see Chapter 1) and the torque on the planet, but such that ignoring self-gravity results in a higher estimate of the migration rate. However, the group only considered the first stable 10 orbits only (with  $Q = 1.6 - 40$ ) without demonstration of the development in disk structure.

In this work, we explore the possibility that disk structure may impact planet migration rate through performing 3D hydrodynamical simulations of Type I migration in stable and borderline stable protoplanetary disks.



## Chapter 3

# Numerical Methods and Early Simulations

### 3.1 ChaNGa - a smoothed particle hydrodynamics code

To investigate the impact of the protoplanetary disk structure on planet migration, we conducted various simulations using ChaNGa, a smoothed particle hydrodynamics (SPH) code originally written for cosmological simulations (Menon, et al., 2015). ChaNGa uses the dynamic load balancing scheme of the Charm++ runtime system, enabling to scale up to half a million processors. The physics modules of ChaNGa are imported from GASOLINE (Wadsley, Stadel & Quinn, 2004) where gravity is calculated using a Barnes–Hut tree (Barnes & Hut, 1986), with hexadecapole expansions of the moments, and hydrodynamics is performed with SPH.

Smoothed particle hydrodynamics code uses discrete particles to model fluid flows. Each particle carries its own physical properties such as mass, pressure, temperature, and moves with the flow. However, any property of the fluid at the particle location can be reconstructed by weighting the value over local particles within smoothing length through a kernel function. Due to the discontinuous nature of the Lagrangian particle method, an artificial viscosity with unphysically large value was introduced to overcome the smooth shock-based problems, ensuring the conservation of mass, energy, momentum and angular momentum. By using spatially and temporally varying smoothing lengths, the resolution increases with rising density though the total number of particles is fixed in the beginning.

For the galactic research presented in Chapter 1, we utilized an adaptive mesh refinement (AMR) code, ENZO, to model an isolated galactic disk in a simulation box of size 32 kpc. The Eulerian grid code creates hierarchy of concentric meshes by concentrating (that is, adding finer meshes) in regions where a given criteria for mesh refinement is achieved (here, the Jeans length is shorter than four cell width). This enables the finest cell size in our simulation reaches 7.8 pc after adding five levels of

refinement. This resolution allows the effective detection of giant molecular clouds (typical radius of 20 pc). However, an AMR code conserves mass, momentum and energy, but not explicitly angular momentum, which is a disadvantage in comparison with Lagrangian SPH code. During a high-resolution galactic simulation which covered a few orbital periods at the outer disk radius, angular momentum is sufficiently conserved. However, modelling the migration of a planet requires potentially tens to hundreds of orbits and the correct computation involves the precise exchange of angular momentum between the gas and planet. Based on concerns that a Eulerian grid code might struggle in this situation, we decided to explore using a particle-based SPH code over a Eulerian grid. The majority of our presented simulations include a million gas particles.

## 3.2 Initial conditions

The initial conditions are generated using the code *diskpy* from [Backus & Quinn \(2016\)](#) with adjustment to create a protoplanetary disk close to hydrostatic equilibrium. By defining the radial temperature profile  $T(R)$ , functional form of surface density  $\Sigma(R)$  and instability parameter  $Q$ , the code computes radial distribution of  $\Sigma(R)$  based on definition of Toomre  $Q$ :

$$Q = \frac{c_s \kappa}{\pi G \Sigma} \quad (3.1)$$

where  $G, c_s, \kappa$  are the gravitational constant, sound speed and epicyclic frequency, respectively. The resultant gas density  $\rho(R, z)$  is estimated, and SPH gas particles are distributed through a 3D disk.

### 3.2.1 Surface density

The Minimum Mass Solar Nebula proposed by [Hayashi \(1981\)](#) suggests the enclosed disk mass within 30 AU is around  $0.01 M_\odot$  with surface density distribution  $\Sigma(R) \propto R^{-3/2}$ . A shallower surface density profile  $\Sigma(R) \propto R^{-1}$  is theoretically predicted by [Bell, et al. \(1997\)](#) based on the viscosity  $\alpha$ -prescription, in which the disk is supposed to have turbulence-ignited viscosity responsible for the redistribution of the angular momentum, resulting in accretion of matter onto the star. Viscosity  $\nu$  is assumed to be proportional to sound speed  $c_s$  and scale height  $H$  of the disk as ([Shakura & Sunyaev, 1973](#)):

$$\nu = \alpha c_s H \quad (3.2)$$

where  $\alpha$  is a dimensionless parameter, ranging from 0 to 1. Though the surface density of planet-forming regions within a few AU has not been probed empirically, larger scales (beyond 20 AU) sub-mm images are consistent with a median profile  $\Sigma(R) \propto R^{-0.9}$  ([Andrews, et al., 2009](#)).



Hence, we choose surface density  $\Sigma$  simply presented in power law form:

$$\Sigma(R) = \Sigma_0 \left( \frac{R}{R_0} \right)^{-\alpha} \quad (3.3)$$

where  $\alpha$  alters with different simulations, and the normalisation  $\Sigma_0$  is the surface density at  $R_0 = 1$  AU, estimated by the desired disk mass to satisfy the minimum value of stability Toomre parameter. Note,  $\alpha$  here is distinct from the viscosity  $\alpha$  mentioned above. Unless clearly stated,  $\alpha$  in this work will refer to the index of the surface density power-law.

In the model in section 4.2 and 4.3, the interior and exterior thresholds for the disk were applied at 0.51 AU and 15.6 AU, creating a region empty of gas directly around the star. As the disk has a viscosity, gas can evolve to fall into this region where it becomes part of the star particle which acts as a sink. While our focus is on the region around the planet (about 5.2 AU), the inner and outer limits of the disk are key to the planet's migration rate. In particular, the locations for the innermost and outermost Lindblad resonance waves (3.15 AU and 8 AU, respectively) must remain on the power-law stretch of the disk density profile for the migration equations discussed in Chapter 2 to be relevant. If the gas density is lower than expected from the power-law in either of these two regions, then the torque balance on the planet will change.

For simulations in section 4.1, the disk extends from 3.6 AU to 12 AU. If planet locates at 8 AU, the edges of the Lindblad waves sit at 5 AU and 12.7 AU respectively, which fit in the disk.

For the outer region of the disk where  $R > R_d$  with  $R_d$  is external radius of the disk ( $R_d = 15.6$  or 12 AU), an exponential cutoff was applied as  $\Sigma_{\text{ex}} = \Sigma(R)e^{-(R-R_d)^2/L^2}$  where the cutoff length was set to  $L = 0.3R_d$ .

### 3.2.2 Temperature of the disk

The temperature profile for the protoplanetary disk is a power-law, decreasing away from the star as:

$$T(R) = T_0 \left( \frac{R}{R_0} \right)^{-\beta} \quad (3.4)$$

where  $\beta$  is the fall-off in temperature and varies between runs and  $T_0$  is the temperature at  $R_0 = 1$  AU. In most simulations,  $\beta$  is chosen to be 1 giving a constant ratio between disk scale height and radius  $H/R$ . In case of section 4.1,  $\beta = 0.5$  is applied for a flatter profile suggested in Beckwith, et al. (1990); Kenyon & Hartmann (1995). In the initial conditions,  $T_0$  is set higher than the minimum temperature at 1 AU  $T_{0,\text{min}}$ , to scale Toomre  $Q$  over the critical threshold for stability with expected disk mass. Typically,  $Q > 2$  is applied before cooling process does its work.

To explore the influence of the disk structure on the planet migration rate, the disk is allowed to cool down to a minimum temperature on the same profile in several orbits. The minimum temperature, is set to a suitably low value to get the desired disk stability. From now on, the term “temperature profile” implies the minimum temperature, at which the state of the disk is determined. This minimum temperature may be lower than expected at the radial distance from the star based on radiation alone. However, as the focus of the project is to explore disk stability and other factors not included in the calculation could affect cooling within the disk (such as dust or magnetic fields), we select values based on the ability to explore the instability parameter space.

The cooling time  $t_{\text{cool}}$  is estimated in a simple approximation related to the angular frequency of the disk,  $\Omega$ :

$$t_{\text{cool}} = \beta_{\text{cool}} \Omega^{-1} \quad (3.5)$$

where  $\beta_{\text{cool}}$  is a constant whose value controls how quickly the disk cools (Gammie, 2001). In addition to Toomre  $Q$ ,  $\beta_{\text{cool}}$  can affect the stability with values above a critical threshold resisting collapse in even gravitationally unstable disks. This is explored further in section 3.3.

### 3.2.3 Star and Planet

All the simulated disks circle a central star of  $1 M_{\odot}$ . Within the code, the star is an N-body particle (rather than a gas particle) and acts as a sink, such that gas particles are removed when approaching within  $R_{\text{sink}} = 0.12 \text{ AU}$  around the star and the properties of that gas (mass, momentum) are added to that of the star.

The planet is treated as a second N-body particle (designated of type ‘star’ in ChaNGa, but this simply removes the particle from feeling gas pressure). The disk is initially allowed to evolve for roughly twenty orbits at the planet position to reach a quasi-steady state, before the planet is added to the simulation. The planet is initialized with a Keplerian circular velocity about the barycenter of the system. The planet mass is either  $0.1 M_{\text{Jup}} \simeq 33 M_{\oplus}$  or  $10 M_{\oplus}$ , depending on the simulation. The planet mass starts equal to that of a gas particle and grows to its final mass over about ten orbital periods at 5.2 AU (see section 3.2.4). For the first simulation result in section 4.1, planet grows up to  $0.01 M_{\text{Jup}} \simeq 3 M_{\oplus}$  at 8 AU.

### 3.2.4 Adjustments to the code for this project

#### The temperature floor

ChaNGa initially allowed gas cooling to a few degrees kelvin. However, while this might be suitable for a cosmological simulation, such a low temperature floor was unphysical in a protoplanetary disk and resulted in the erasure of the temperature

gradient. (This can be seen in our early test runs in Figure 3.2.) To combat this, a minimum temperature floor with a radial dependence was added to the code so that the gas could cool as described in section 3.2.2. The floor is defined by specifying the temperature  $T_{0,min}$  at 1 AU in the simulation parameter file and the required temperature radial gradient (still currently hardwired into the code, so recompiling is necessary).

### Planet growth

An early issue that was encountered is that the planet's motion through the disk changed during the first few orbits. This was due to the properties of the disk altering as the gas cooled. The result was that the planet's initial position and velocity (once the disk had reach equilibrium) was no longer constant between runs.

To combat this issue, the planet was added after the simulation had started, once the disk has performed about 20 orbits at the planet's planned position. The planet was then added with the same mass as a gas particle, so not to create a sudden shock to the disk distribution. Over a further ten orbits, the planet grew to its designated size. Over that period, the planet's orbit was not fixed and migration could begin. However, the time for planet growth compared to the rest of the simulation is small, so this epoch could be excluded from the analysis. The capacity for particle growth was added to ChaNGa for this project.

All changes were made with advice from Professor James Wadsley (McMaster University) and Professor Tom Quinn (University of Washington) who are developers of ChaNGa. The actual code development was done with supervisor, Elizabeth Tasker, and testing performed as part of this doctorate.

## 3.3 Initial runs

Before exploring the the impact of disk instability on the migrating planet, we performed an initial set of runs to test how the protoplanetary disk evolved under different choices for the cooling parameter.

### 3.3.1 Effect of cooling rate on disk stability

As described in section 3.2.2, the cooling rate of the gas in the disk is controlled by the factor  $\beta_{cool}$ , which relates the cooling time,  $t_{cool}$  to the angular frequency of the disk,  $\Omega$ . The linear analysis of Gammie (2001) suggests a threshold value for  $\beta_{cool}$  for fragmentation in a 2D disk is  $t_{cool} \leq 3\Omega^{-1}$ , i.e  $\beta_{cool,crit} = 3$ . However, the critical value of  $\beta_{cool}$  has been shown to be dependent on the disk properties, e.g. disk mass (Rice, et al., 2003), the equation of state (Rice, Lodato & Armitage, 2005) and steepness of the surface density distribution (Meru & Bate, 2011). This leads to much longer cooling

times ranging from  $5\Omega^{-1}$  to  $13\Omega^{-1}$ . The artificial viscosity in SPH simulation can also affect the estimation of the cooling rate, causing the critical  $\beta_{\text{cool}}$  to be even as large as 20 (Meru & Bate, 2012).

These widely varying values makes it difficult to determine the appropriate value of  $\beta_{\text{cool}}$  to use in these simulations from analytical considerations alone. We therefore ran four test simulations to determine the impact of  $\beta_{\text{cool}}$  on the disk evolution. Each disk had a total gas mass of  $0.05 M_{\odot}$  and evolved the gas using a different cooling rate,  $\beta_{\text{cool}} = 20, 13, 11.5,$  and  $10$ .

These tests were run prior to the introduction of the temperature floor and planet growth discussed in sections 3.2.2, 3.2.3 and 3.2.4. In this stage, the disk was allowed to cool freely with no constraints from a minimum temperature profile. The disk evolved without the planet for about 20 orbits at a radius of 5 AU. A planet of mass  $0.01 M_{\text{Jup}}$  (Jupiter mass)  $\simeq 3 M_{\oplus}$  was then inserted at 5 AU and interacts with the gas disk.

Figure 3.1 shows the surface density of the protoplanetary disks for different values of  $\beta_{\text{cool}}$ . Left-to-right and top-to-bottom,  $\beta_{\text{cool}}$  decreases in value, corresponding to a steadily more unstable disk. The time of the simulation is just as the planet has been added to the disk, after approximately 20 orbits at the planet position. Corresponding to these four disks are radial profiles for the gravitational instability parameter, Toomre Q, surface density and temperature shown in Figure 3.2.

All four disks have the same average radial surface density distribution, which is much larger than the MMSN (denoted by the dotted line in the middle panel). However, the difference in the value for  $\beta_{\text{cool}}$  leads to different temperature profiles and results in a variety of structures in the disks.

The fastest cooling process  $\beta_{\text{cool}} = 10$  (lower right in Figure 3.1) produces the most unstable disk with lots of fragmentation and the formation of dense clumps. The two rich structure disks (spirals but few or zero clumps) belong to  $\beta_{\text{cool}} = 11.5$  and  $13$  (lower left and upper right), but the regions around the planet (denoted by a red dot) does not differ significantly. The most stable disk matching  $Q > 1$  (blue line in the top panel in Fig. 3.2) shows little structure in the gas, despite having the same mass as the other discs. Although the Toomre Q of the other three unstable disks are all borderline unity, the difference in regions around planet is noticeable and the global disk appears to show quite a different range of instability.

Based on these results, a value for  $\beta_{\text{cool}} > 13$  strongly increases the gravitational stability of the disk. As the disks we want to explore for this work are at least borderline gravitationally unstable, we did not wish to use a cooling time so long that the disk remained supported. Based on these simulations,  $11 < \beta_{\text{cool}} < 13$  would provide a borderline stable disk, where the disk instability does not drop low enough to cause

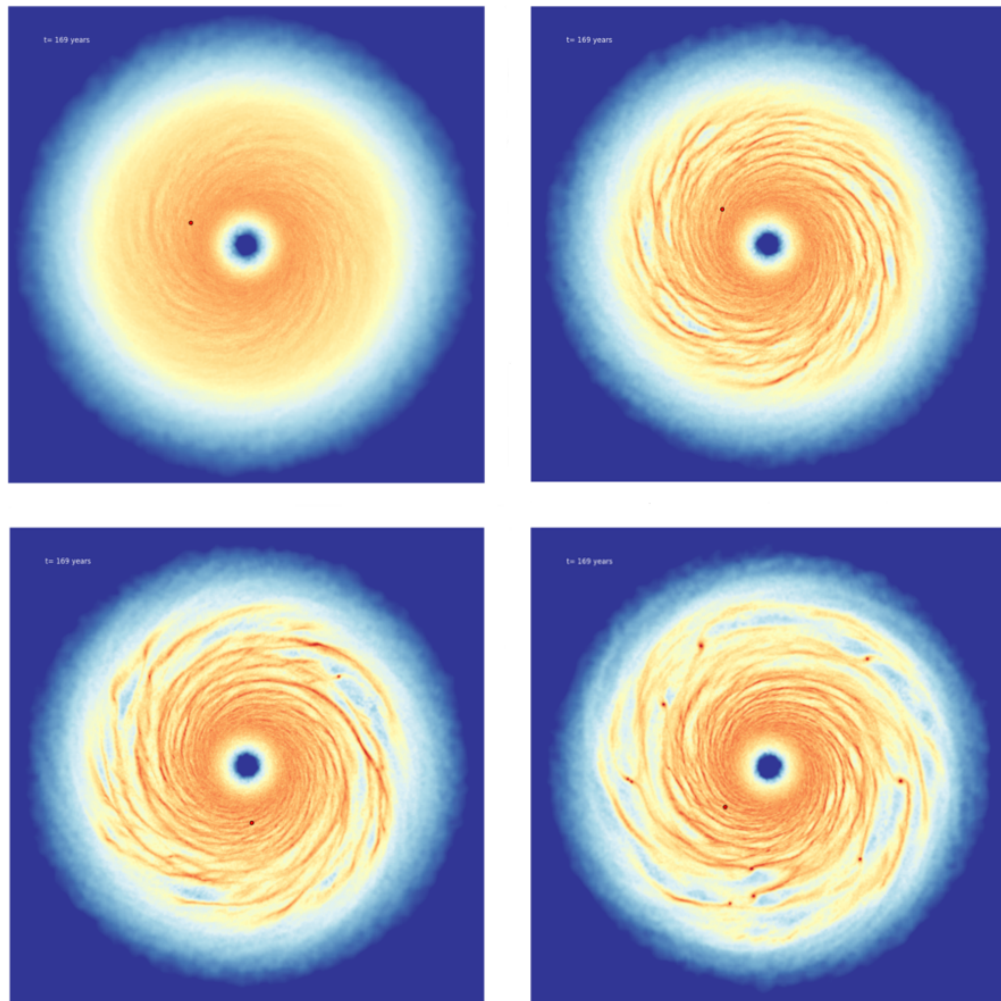


FIGURE 3.1: Distribution of surface density of 4 disks, in which from left to right, top to bottom, the instability of the disk is expected to increase, corresponding to cooling parameter  $\beta_{\text{cool}} = 20, 13, 11.5,$  and  $10$ . The red dot indicates the planet location.

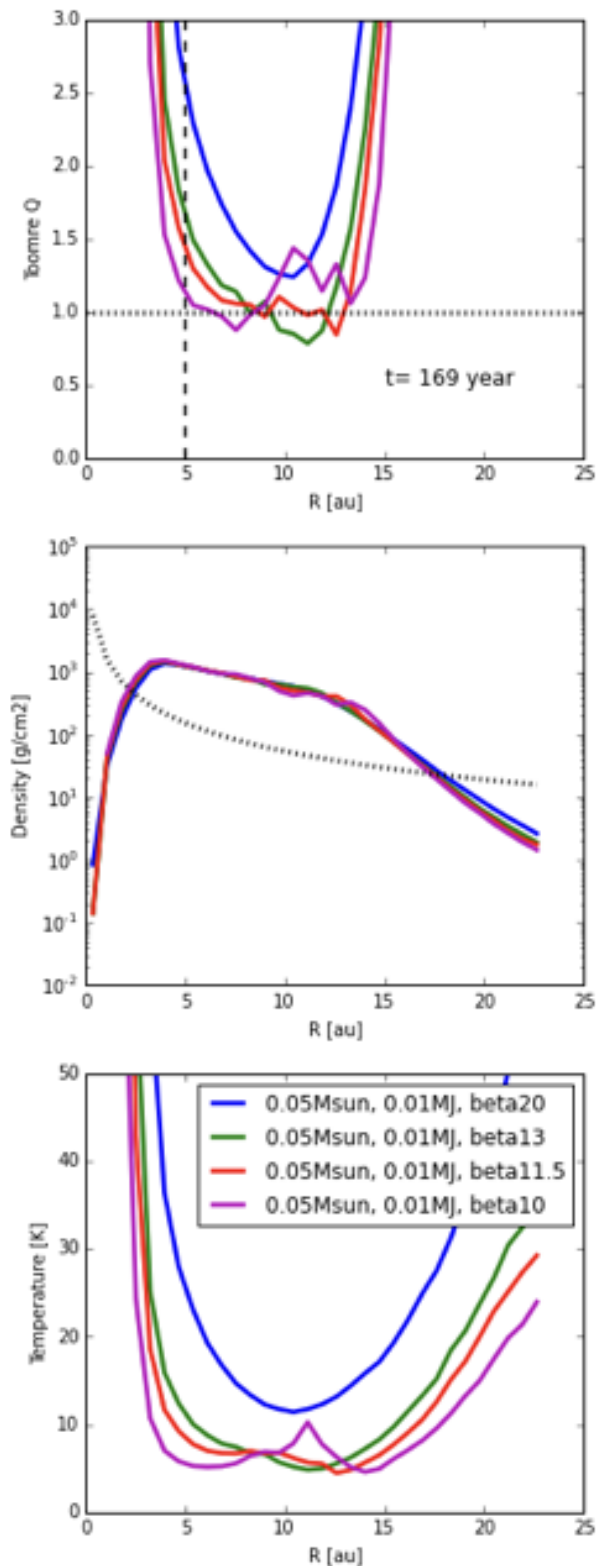


FIGURE 3.2: Toomre  $Q$ , surface density and temperature profiles of various protoplanetary discs (top to bottom). In the top plot, horizontal dotted line indicates the critical value of stability and the vertical dashed line estimates the position of the planet at the beginning. In the middle plot, the dotted line presents the MMSN surface density.

fragmentation. As the goal is to look at the impact of disk structure on Type I migration for a planet formed via core accretion, not to form planets via disk instability, the  $\beta_{\text{cool}} = 10$  disk is too unstable.

In fact, these early runs were implemented before the introduction of the temperature floor discussed in section 3.2.2. Once the floor had been implemented to prevent the extremely low temperatures visible on Fig. 3.2, we were able to raise the value so that  $\beta_{\text{cool}} = 8$  achieve the same results as the  $\beta_{\text{cool}} = 11.5$  and 13 disks. For this reason, our runs focused on using  $\beta_{\text{cool}} = 8$  and stability was varied by different values of the total disk mass.

### 3.3.2 Migration in an unstable disk

With the four disks prepared, we were able to test if the disk instability is likely to make a strong difference to the planet migration rate. Each of the disks was further allowed to evolve and the change in the orbital radius of the planet is plotted in Figure 3.3. The dashed line indicates the theoretical estimate by Tanaka, Takeuchi & Ward (2002) as a response to the torque in Equation 2.9 for each planet migration in the matching color.

The three unstable disks corresponding to  $\beta_{\text{cool}} = 10, 11.5$  and 13 all show a strong deviation from the analytical prediction in their path towards the star. However, the planet in the most stable disk ( $\beta_{\text{cool}} = 20$ , blue line) seems to experience a smooth migration, reasonably close to the predicted path, and gradually is sent to the host star without remarkable event. In contrast, the spiral structures in the semi-stable disks ( $\beta_{\text{cool}} = 13$  and 11.5, green and red lines respectively) may sweep past the planet and drive it move outward sometimes on its way toward the star. As the  $\beta_{\text{cool}} = 11.5$  model shows a lower  $Q$  near planet location (Fig 3.2), the planet orbital radius fluctuates strongly, especially at around 600 years. The existence of clumps in the most unstable disk,  $\beta_{\text{cool}} = 10$  causes a scattering event between the embedded planet and the clump in the disk, knocking it far away from the initial position. This is an extreme case that we do not expected to be common in reality, as this level of fragmentation is not expected in most disks (as discussed in Chapter 2).

These runs clearly demonstrate that gravitational instability can have a sizeable impact on the planet migration. The next part of this thesis was to consider the magnitude of this effect in comparison to analytical expectations.



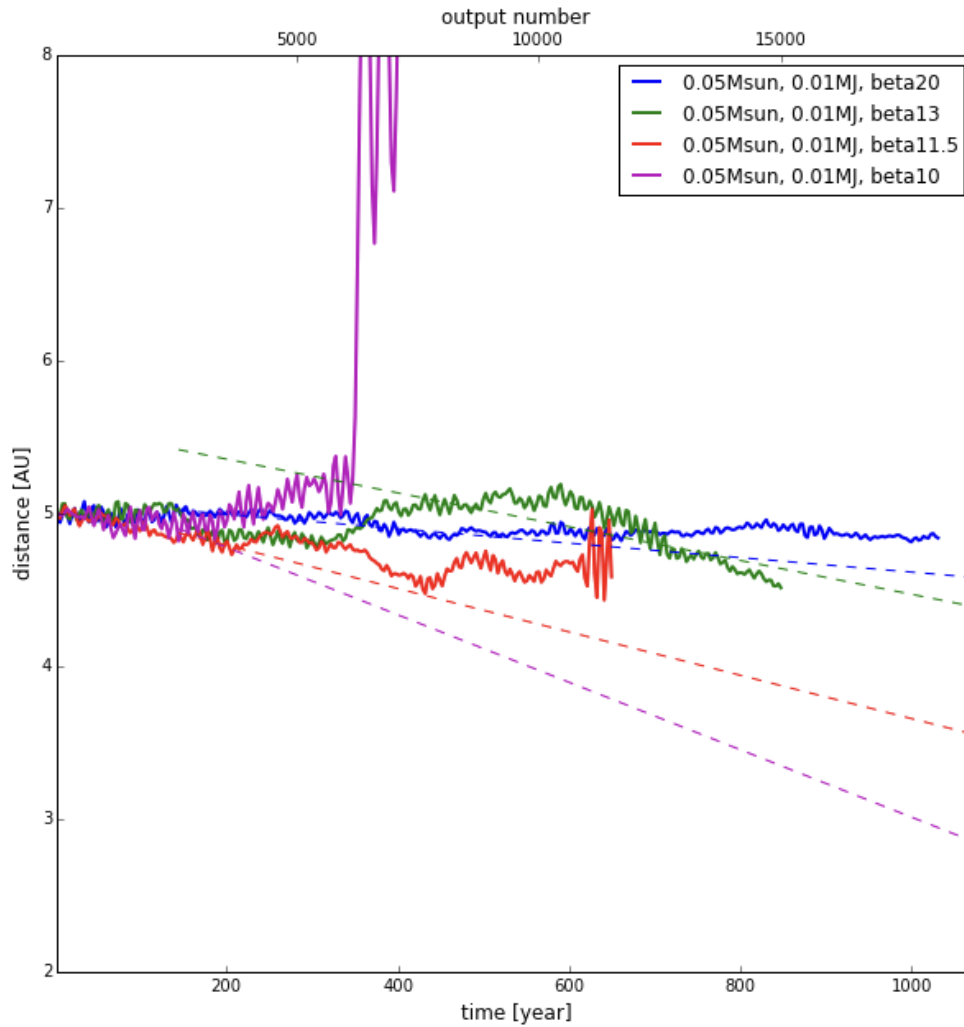


FIGURE 3.3: The variation of planet orbital radius in protoplanetary disks. The straight lines in matching colour present theoretical estimation of type I migration timescale.



## Chapter 4

# Simulating Disk Instability with Migration

### 4.1 First simulation results

Based on the simulations presented in Chapter 3, we considered three protoplanetary disks that were sufficiently stable to avoid the formation of dense clumps of gas and scattering of the planet. The three disks are referred to throughout this section as **Stable**, **Semi-stable** and **Semi-stable Heavy** with the disk parameters shown in Table 4.1.

Figure 4.1 shows the radial distribution of the Toomre Q parameter, surface density and temperature of the three different protoplanetary disks when the planet had just finished growing, as described in section 3.2.3. The disk owns a surface density profile in form of  $\Sigma \propto R^{-1}$  and extends from 3.6 AU to 12 AU, followed by an exterior cutoff. The planet mass is the same as in the simulations presented in Chapter 3 at  $0.01 M_{\text{Jup}} \simeq 3 M_{\oplus}$ , but the planet's initial position is now at 8 AU. This shift was because if planet position is 5 AU, the location of the innermost Lindblad resonance of sits at  $R_{\text{ILR}} = 3.15$  AU (Eq. 2.3) and fell within the inner cut-off of the surface density profile. As mentioned in section 3.2.1, this risks affecting the exchange of angular momentum between the planet and a less dense region of gas, changing the net torque. To ensure both the inner and outer Lindblad resonance locations sit on the power-law section of

Name	Mass $M_{\text{disk}}$	Temperature floor
Stable	$0.04 M_{\odot}$	$50.0 R^{-1/2}$
Semi-stable	$0.04 M_{\odot}$	$50.0 R^{-1}$
Semi-stable Heavy	$0.08 M_{\odot}$	$50.0 R^{-1/2}$

TABLE 4.1: Disk parameters used in the simulations presented in section 4.1. The temperature floor profile applies to the minimum temperature allowed for cooling as described in section 3.2.2. (The same exponent, either  $-1/2$  or  $-1$ , is also used for the initial conditions for the gas temperature.)

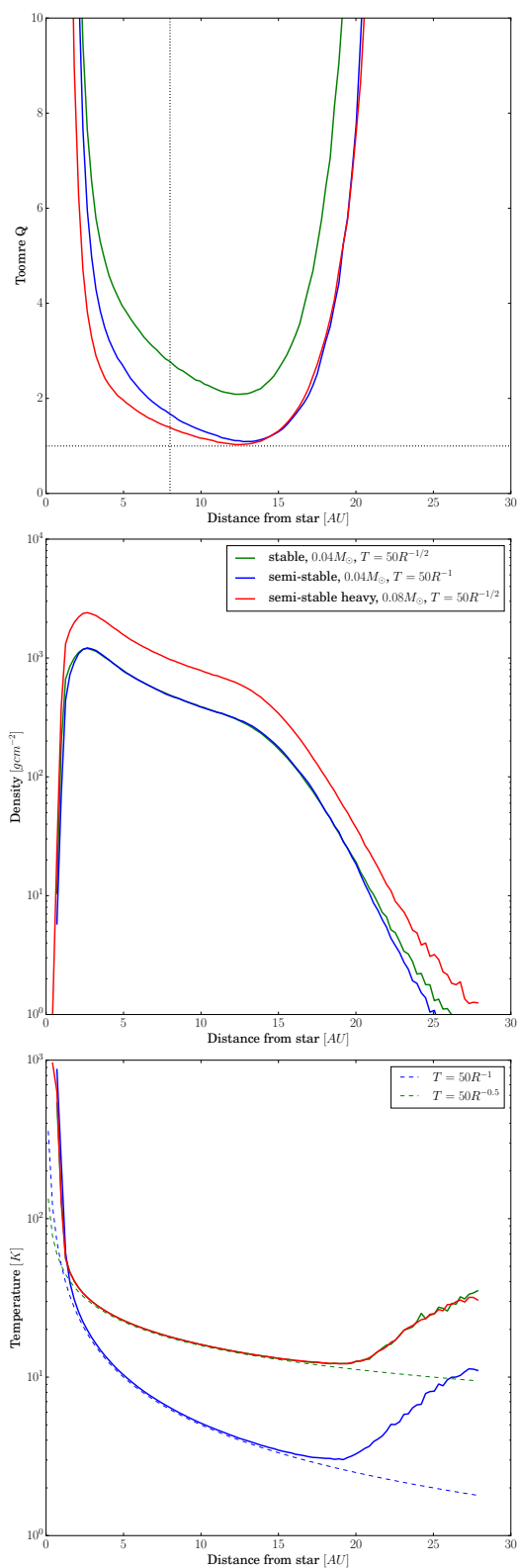


FIGURE 4.1: Toomre  $Q$ , surface density and temperature profiles of the three protoplanetary discs in Table 4.1 (top to bottom). In the top plot, the horizontal dotted line indicates the critical value of stability and the vertical dashed line estimates the position of the planet at the beginning of the simulation. In the bottom plot, the dashed line indicates the location of the cooling floor.

the protoplanetary disk, the planet was moved outwards from 5 AU to 8 AU for this section. This shifted the inner Lindblad resonance location to 5 AU

As shown in Table 4.1, the protoplanetary disks vary in mass and in the form of their temperature profile. The three disks are designed to share one common property with one of the other two runs in order to examine the impact of the varying factors on the planet migration. **Stable** and **Semi-stable** disks (green and blue lines, respectively, in Figure 4.1) have the same disk mass but different temperature profiles, giving the two runs an identical surface density profile shown in the middle panel of Fig. 4.1, but a different stability profile as shown in the top panel of Fig. 4.1. The Toomre Q parameter of **Stable** is approximately 3, well above the critical value of 1.0, presenting the disk with little structure. Considering **Stable** and **Semi-stable Heavy** (green and red lines, respectively), they have the same temperature profiles but now different disk masses, giving different density profiles and Toomre Q values. Finally, **Semi-stable** and **Semi-stable Heavy** have different disk masses and different temperature profiles, but similar stability.

Technically, all runs have an instability parameter Q larger than 1, especially around planet position (8 AU), which means fragmentation is minimal. However, the face-on distribution of the surface density for the whole disk in Figure 4.2 illustrates visible difference in the disk structure. The **Stable** simulation (left-hand image in Fig. 4.2) shows the least structure with a homogeneous distribution of gas in the stable disk, while **Semi-stable** and **Semi-stable Heavy** (middle and right images) have similar structures with flocculent spiral arms, although **Semi-stable Heavy** is denser due to its high mass. In all three runs, the Lindblad waves emanating from the planet (denoted by a red dot) are visible, but most discernible in the massive **Semi-stable Heavy** run (see Fig. 4.4 for images of Lindblad torque). The Lindblad and disk spiral appear similar in strength in those two cases, suggesting that the disk instability and Lindblad resonance may have a competing influence in both disks.

Figure 4.3 shows the movement of the planet in the three disks. In all cases, the planet orbit remains slightly elliptical. This is strongest right at the beginning of its life, while the planet is still light and growing from the size of a gas particle. Once it reaches its  $0.01 M_{\text{Jup}}$  mass, its motion is rapidly damped by the gas. This elliptical orbit is also found in simulations of [Ayliffe & Bate \(2010\)](#) but its eccentricity is smaller and almost unchanged on account of very light disk ( $0.005 M_{\odot}$ ). In all three cases, the planet migrates faster than the analytical expectation, shown by the solid line in the matching color ([Tanaka, Takeuchi & Ward, 2002](#)).

Sitting within the most stable and homogeneous disk (**Stable**), the planet is on the trend to travel toward the star at the slowest rate and migrates smoothly without any noticeably strong deviation. **Semi-stable** and **Semi-stable Heavy** have similar Q and similar spiral structure, but the heavier disk results in a bouncier path (seen in torque

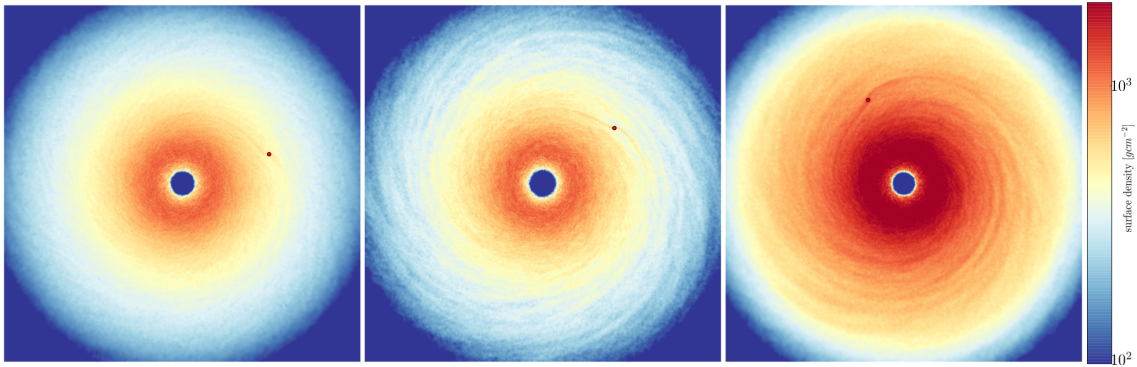


FIGURE 4.2: The 2D distribution of surface density of various disks at different stability degrees and red dot indicates the planet's location. From left to right, the disk are respectively **Stable** light disk, **semi-stable** light disk, **Semi-stable Heavy** disk. The red dot indicates the planet location in the disk.

plots next), showing short periods of outward motion even while having an overall inward progression (e.g. at 700 - 1000 years). The difference in disk mass and temperature profile at planet position (Figure 4.1) between the **Semi-stable** and **Semi-stable Heavy** runs is theoretically predicted to change the rate of migration, but the interaction between the disk structure and planet seems to be important in creating the match between the red and blue lines after 800 years in Figure 4.3. This suggests that the disk structure may actually be dominating the Lindblad resonances. This may be particularly true in the case of **Semi-stable Heavy**, compared with **Semi-stable**, which shows the largest deviation from the analytical path, despite the resonance waves visually looking similar in Fig. 4.2.

To more fully understand how the structure of the disk is altering the expected migration rate of the planet, we need to look directly at the cause of planet migration: the exchange of angular momentum and torque on the planet. Figure 4.4 shows the 2D distribution of torque around planet location. Although Figure 4.2 revealed visible Lindblad waves in all three runs, the torque on the **Semi-stable** disk is shown most clearly of the three in the middle panel of Figure 4.4. The less visible torque is not surprising in the homogeneous **Stable** disk (left), as the Lindblad waves also appeared only weakly in Figure 4.2, and the disk itself generally showed little structure. It does suggest that the Lindblad torque is more important relative to the disk structure than for the **Semi-stable Heavy**. This is consistent with Fig. 4.3, which shows the greatest deviation from the analytical migration rate (which should be controlled by the Lindblad torques) for the **Semi-stable Heavy** disk.

Figures 4.5 and 4.6 plot the net torque on the planet averaged over 1 orbit then normalized by either a constant amount of  $-10^{36} \text{ g cm}^2 \text{ s}^{-2}$  for all simulations, or the averaged torque  $\tau_{avg}$  to inspect how torque changes relative to early torque.  $\tau_{avg}$  is calculated over first 15 orbits after planet's development completes. We excluded a region equal

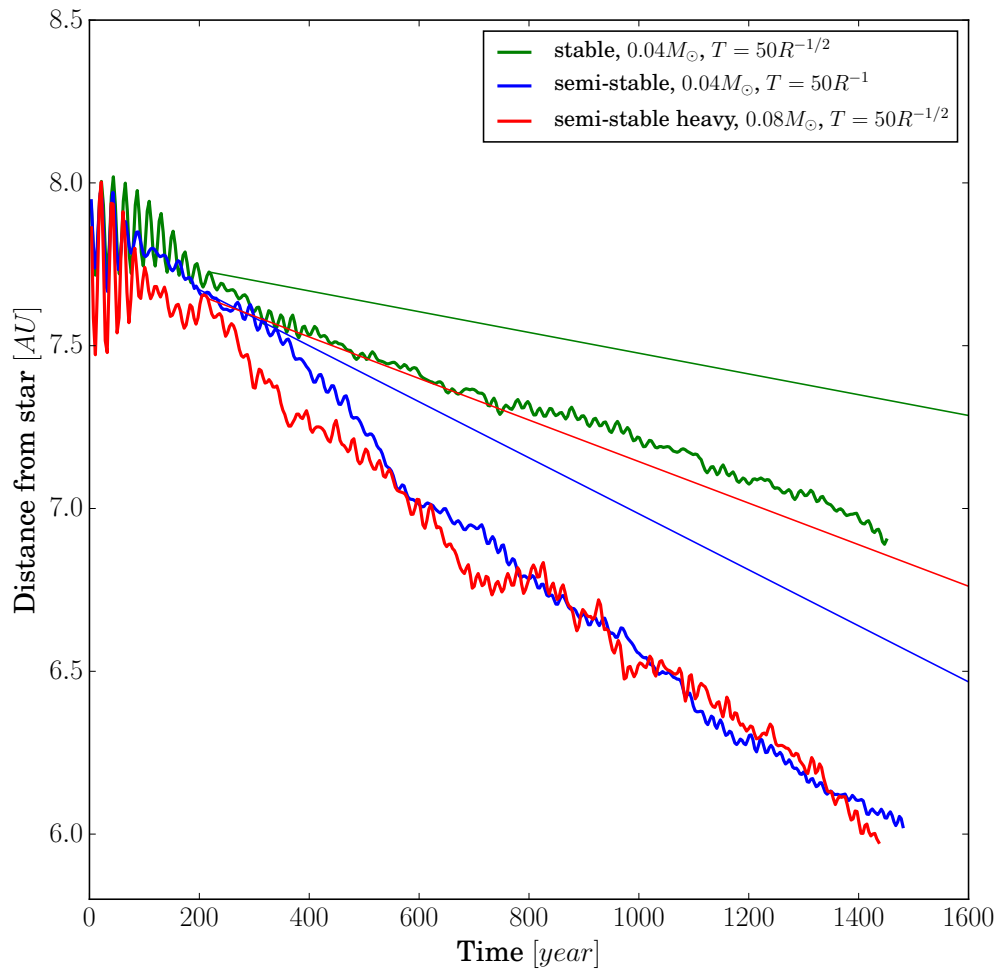


FIGURE 4.3: The variation of planet orbital radius in the protoplanetary disks. Solid line indicates the analytical expectation of the migration based on Eq. 2.9

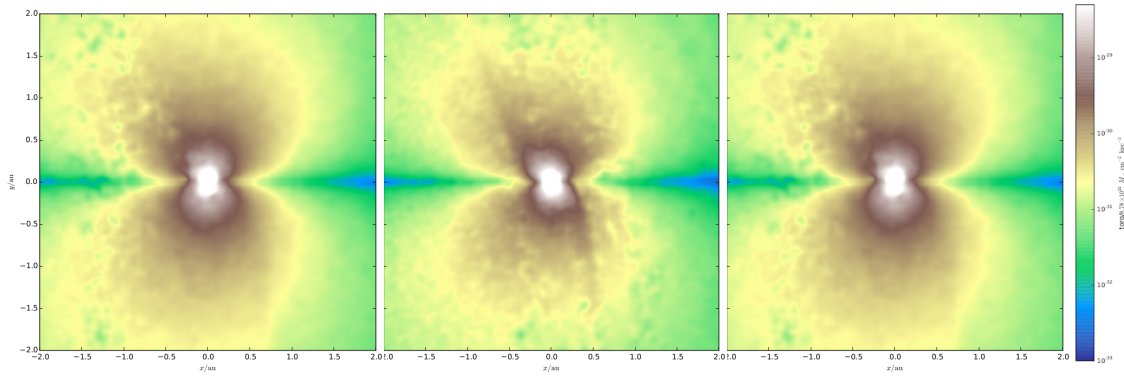


FIGURE 4.4: The 2D distribution of torque around planet. From left to right, the disk are respectively Stable light disk, Semi-stable light disk, Semi-stable Heavy disk

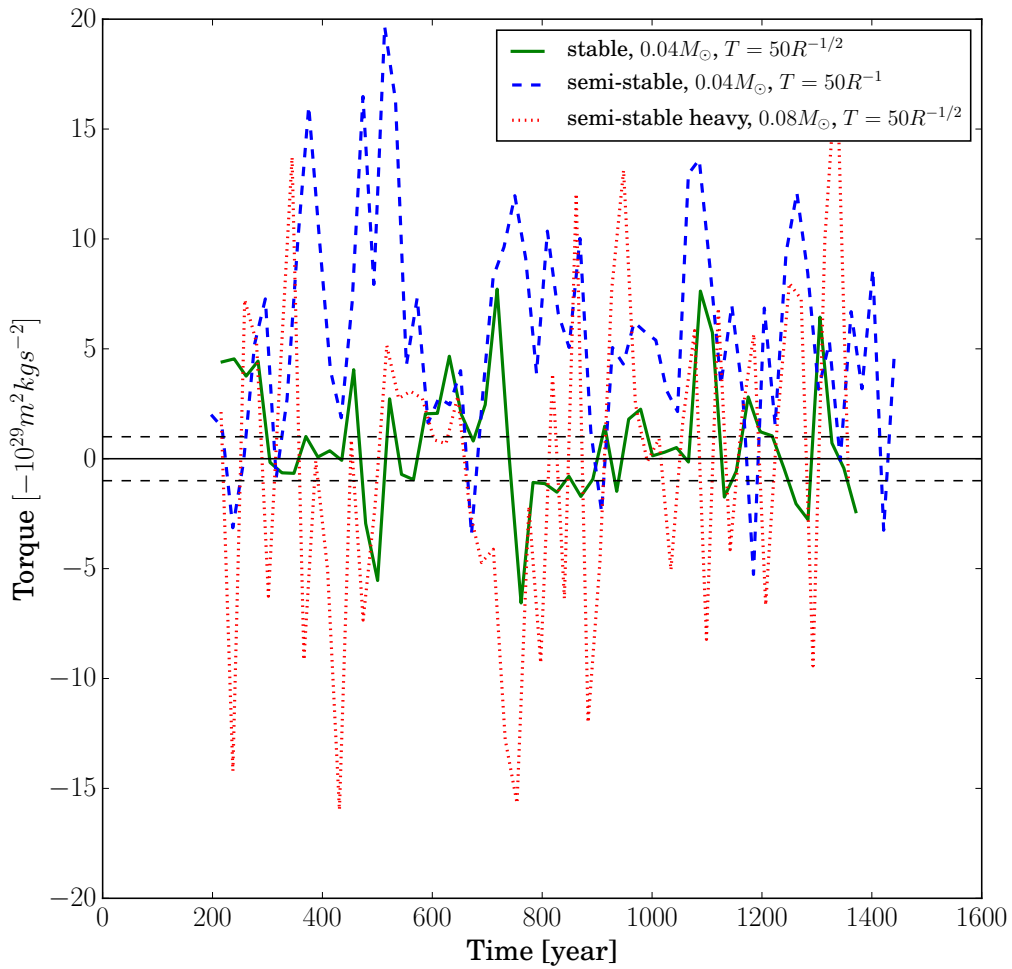


FIGURE 4.5: The net torque (excluding Roche sphere) averaged over 1 orbit then normalized by  $-10^{29} \text{ kgm}^2\text{s}^{-2}$ .

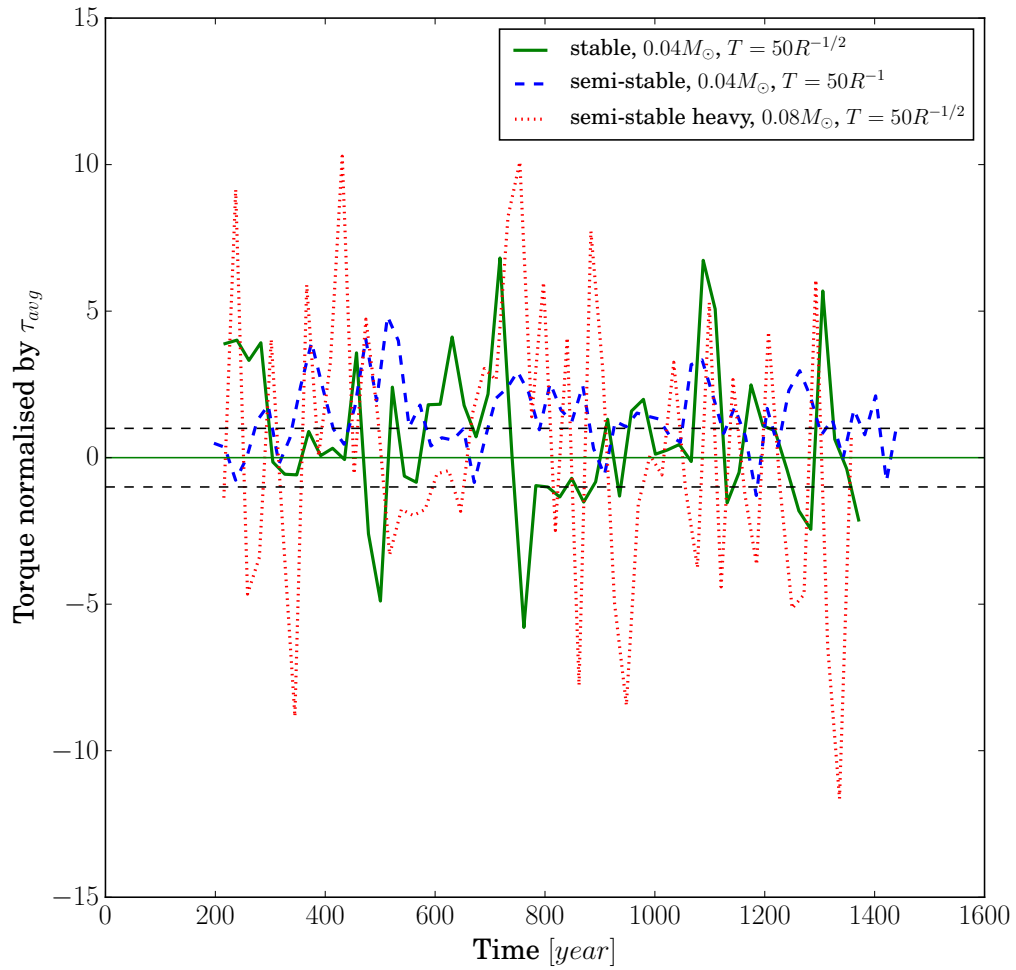


FIGURE 4.6: The net torque (excluding Roche sphere) averaged over 1 orbit then normalized by  $\tau_{avg}$  calculated over first 15 orbits after planet's development completes.

to the planet's Roche sphere around planet's position to avoid the local domination of gravity from the planet as assumed in the analytical calculations and simulations of Ward (1997); Tanaka, Takeuchi & Ward (2002); Bate, et al. (2003). Here, the size of the Roche sphere is defined by the Hill radius:

$$R_{\text{Hill}} = R_p \left( \frac{M_p}{3M_s} \right)^{1/3} \quad (4.1)$$

Based on the linear analytical calculation in Eq. 2.9, we naively expect **Stable** to have the weakest torque, **Semi-stable Heavy** to have the middle torque strength and **Semi-stable** to have the strongest torque. These correspond to the gradients of the straight lines in Figure 4.3. On the other hand, based on the actual migration rates in Figure 4.3, we might guess **Semi-stable** and **Semi-stable Heavy** have similar torques as they match the migration rate at later times. Looking at Figure 4.5, the **Stable** disk (green solid line) does show the weakest torque as expected. It also shows smallest fluctuations in torque, which is consistent with the weak disk structure having minimal impact on the planet. Notably, in Figure 4.6 (when normalized by the early averaged torque), this fluctuation amplitude is similar to **Semi-stable** (blue dashed line), which implies both runs show a similar degree of variability compared to early torque over their migration. During a given time period, **Stable** seems to show slightly less peaks and troughs than the other two runs. This is consistent with the smooth path inward towards the star.

The more unstable **Semi-stable** and **Semi-stable Heavy** disks show high fluctuations compared to the **Stable** disk, indicating that the disk structure is playing an important role in planet motion. Although **Semi-stable** and **Semi-stable Heavy** migrate at similar rates, **Semi-stable Heavy** has a much wilder ride, with very noisy torque in both Figure 4.5 and 4.6 that reflects the more jagged path in Fig. 4.3 and the stronger role disk structure appears to be playing compared with **Semi-stable**. This demonstrates that the Toomre Q parameter alone does not control planet motion. Presumably, these differences are because there is more gas mass in the spirals, giving a strong interaction between the massive disk and planet which dominates the Lindblad torques more easily. Such structures may work similarly to short-lived planet traps, in that they alter the torque on the planet. Notably, however, these "traps" cause an increased velocity of the planet towards the star, as opposed to the reverse.

In order to compare to analytical calculation, Figure 4.7 presents the net torque averaged over 20 orbits in comparison with linear estimation taken from Tanaka, Takeuchi & Ward (2002) indicated by dashed lines in matching colors. How large the deviations of the averaged torques from analytical lines are compatible with the divergences of the planet paths in corresponding disks. The smallest departure of the **Stable** line, which is also found in Fig. 4.5, is expected from its least diverging path in Fig. 4.3,



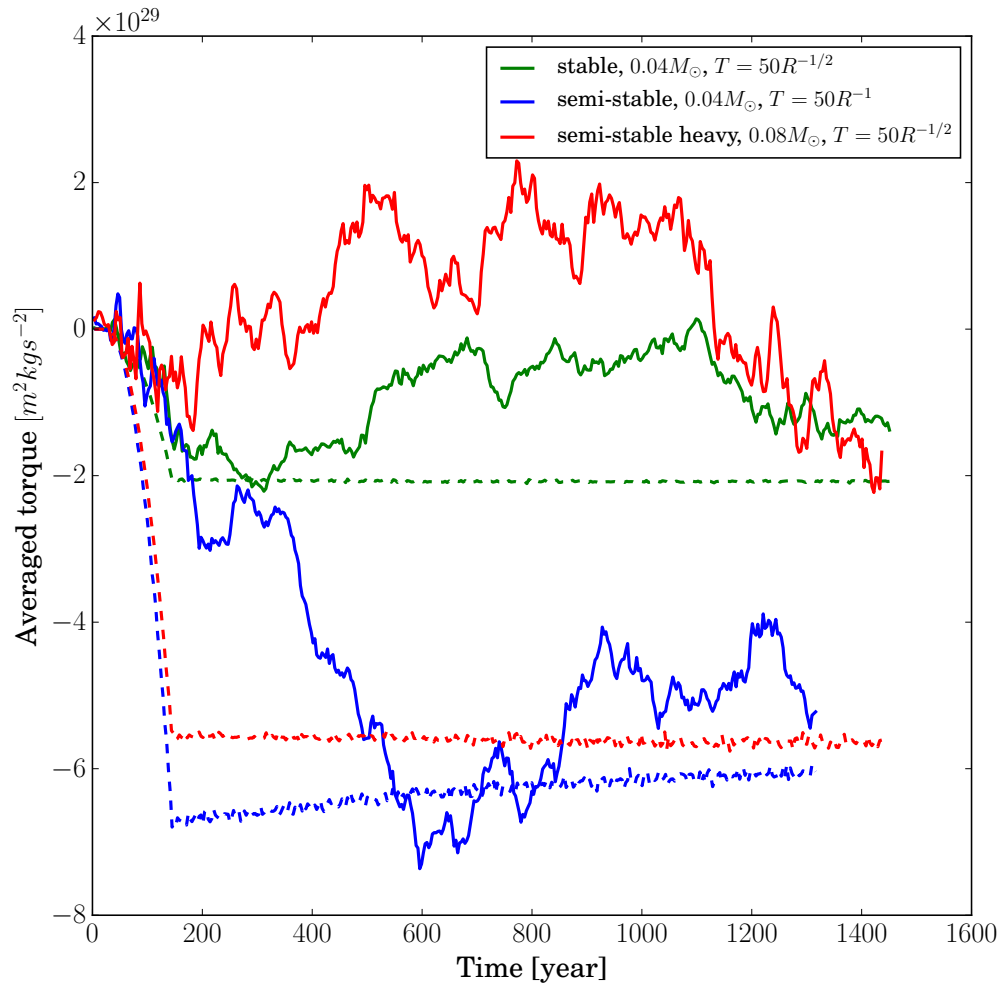


FIGURE 4.7: The net torque (excluding Roche sphere) averaged over 20 orbits in comparison with linear estimation (dashed lines in matching colors) taken from [Tanaka, Takeuchi & Ward \(2002\)](#).

showing minimal impact of little structure disk. Its magnitude also varies slightly, advocating a relatively smooth journey toward host star due to weak impact of the disk.

The noticeable variations of the **Semi-stable** and **Semi-stable Heavy** lines agree with the bouncy migration paths of planets in the unstable disks. The **Semi-stable Heavy** experiences remarkable fluctuation and flips sign during the migration, accordant with the reversals in the way toward star. Despite the different radial profiles, these two unstable disks have comparable theoretical values. However, the massive **Semi-stable Heavy** (red line) departs greatly from the analytical line, while the **Semi-stable** (blue line) fluctuates around its own, explaining the most clear patterns of the Lindblad torque in Fig. 4.4. This emphasizes, again, the dominant power of disk structure to Lindblad resonances in the massive **Semi-stable Heavy**. The decrease in analytical value of **Semi-stable** results from the faster migration rate in compared with **Stable** and the lower surface density than **Semi-stable Heavy**.

Although the fact that the effect of the disk structure on the planet is reflected in the movement of the planet is remarkable, the fluctuation of the elliptical orbit is not definitely fully understood. A major question was whether all the orbital path differences from the analytical expectation were entirely due to disk structure. To investigate this, we performed simulations of a much lighter disk that should be free of gravitational instabilities.

## 4.2 Matching Type I migration

### 4.2.1 Low-mass planet in a homogeneous light disk

In order to reproduce a standard Type I migration, we tried to mimic the light disk in [Ayliffe & Bate \(2010\)](#), in which the planet interacts with gaseous disk and the calculated average torque is close to that predicted from linear analysis. The initial conditions are generated as in section 3.2 with the following adjustments: The disk mass is set to  $\approx 0.005 M_{\odot}$ , with the surface density dependence with radius given as  $\Sigma \propto R^{-1/2}$ , i.e.  $\alpha = 1/2$ . The radial profile of temperature is determined by  $T = 390 R^{-1}$  K, i.e.  $\beta = 1$ . The planet is embedded in the disk at 5.2 AU and increases from  $0.00165 M_{\oplus}$ , as light as a gas particle, to either  $10 M_{\oplus} \approx 0.03 M_{\text{Jup}}$  or  $33 M_{\oplus} \approx 0.01 M_{\text{Jup}}$  in about 10 orbits, depending on the simulation. The whole system orbits a solar-mass star as before.

Figure 4.8 shows the radial profile of the Toomre Q parameter, surface density and temperature of the disk during the migration of the planet. When inserting the planet, the disk has reached its equilibrium, so the stability (top panel) and temperature (bottom panel) do not change significantly over time. The disk remains stable during the

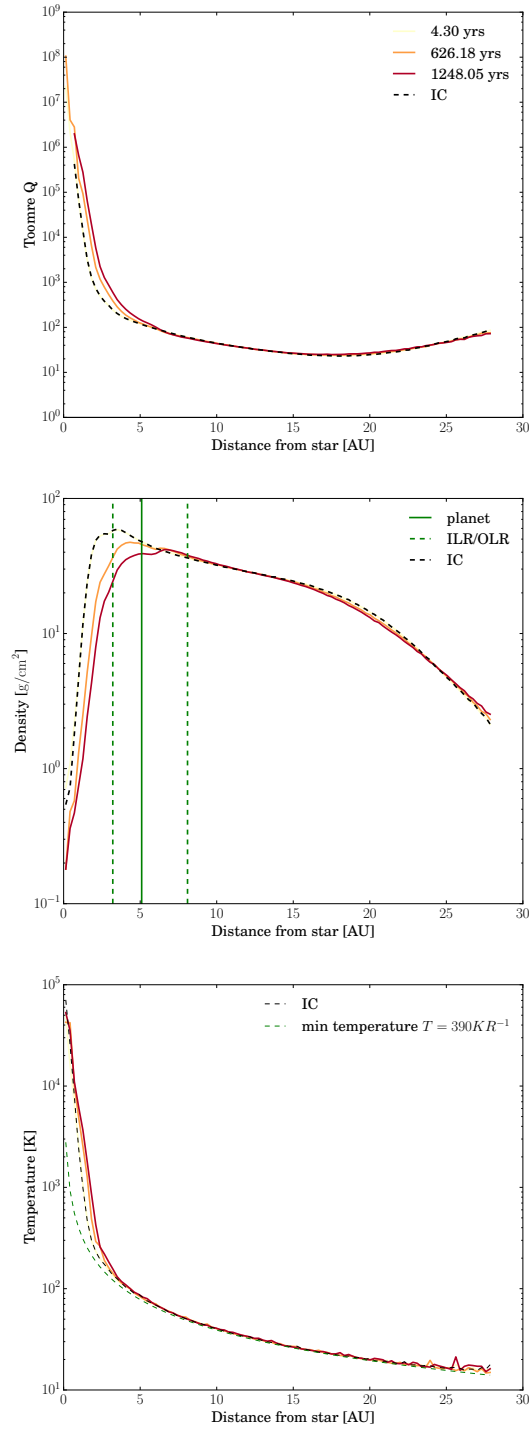


FIGURE 4.8: Top to bottom: Radial distribution of the gravitational instability parameter (Toomre  $Q$ ), surface density and temperature of the disk with mass of  $0.005 M_{\odot}$ . Black dashed lines indicate disk profiles before inserting planet but after the disk settled. The vertical lines in middle panel indicate locations of the planet (solid) and the innermost/outermost Lindblad resonances (dashed left/right) at the last output, i.e. 1248 years. Green dashed curve in bottom panel denotes the minimum temperature. The Toomre  $Q$  (top) is always above 1.

simulation and shows little structure as  $Q$  is always much larger than the critical value, 1.0. Because the star is set to a sink particle and sits within a viscous disk, the inner edge of the surface density moves slowly further from the star as material is accreted, while the outer part is unchanged. The vertical lines in middle panel illustrate the positions of the planet (solid line) at the end of the simulation, i.e. 1248 years  $\approx$  100 orbits, and its innermost and outermost Lindblad resonances (dashed lines). By the end of the migration, the innermost Lindblad resonance falls into the lower density regions, which can cause underestimation of the interior torque and impact the migration.

As expected from the large  $Q$ , Figure 4.9 illustrates that the 2D surface density distribution has an indistinct structure. In the homogeneous disk, the Lindblad waves ignited by both the planets (denoted as a green dot) are recognizable, and denser for the bigger planet, predicting a larger exchange of angular momentum with the gas disk.

Figure 4.10 presents the evolution of the planet orbit radius and mass during its migration. The increase in planet mass in a few early orbits results in increasing interaction with the gas disk, leading to slightly more elliptic orbit. In the first 20 orbits, the planet completes the mass growth and settles down (this is more strongly visible in the planet torques below). This is equivalent to the early stabilization time after introducing planet also noted by [Ayliffe & Bate \(2010\)](#). Both  $10 M_{\oplus}$  and  $33 M_{\oplus}$  planets (green and blue lines, respectively) smoothly migrate inward toward the star without any change in direction. The fluctuation of the orbit radius (that is, the slight ellipticity) is even and tends to diminish after a few hundred years as the gas damped the eccentricity, but the heavier planet keeps a slightly larger eccentricity as its motion is more difficult to damp on account of the planet's higher mass. What is more difficult to explain is that the  $33 M_{\oplus}$  planet migrates slightly slower than the  $10 M_{\oplus}$  one, in contrast with theoretical prediction. One possibility is that the higher eccentricity of the heavier planet is weakening the torques on the planet.

The torque on the planets is shown in Figures 4.11 and 4.12, displaying the torque variation during the migration of two planets,  $10 M_{\oplus}$  and  $33 M_{\oplus}$ . To avoid the domination of local gravity, the material within Hill radius near the planet is assumed not to exert torque on planet and gas particles within this region are excluded from the calculation (cyan thin line and blue line) ([Ward, 1997](#); [Tanaka, Takeuchi & Ward, 2002](#)). In addition, the averaged torque beyond  $0.5$  and  $1.5 R_H$  are also presented (green and red lines, respectively) to depict the uncertainties of the torque. The average torque is averaged since the planet is introduced. Furthermore, theoretically and numerically approximated torque are also displayed for comparison (black solid and dashed lines) based on estimations by [Tanaka, Takeuchi & Ward \(2002\)](#) in Equation 2.9 and [D'Angelo & Lubow \(2010\)](#) in Equation 2.12. The upper and lower panels in each figure depict the same torque evolution, but the lower panel in both figures is on the

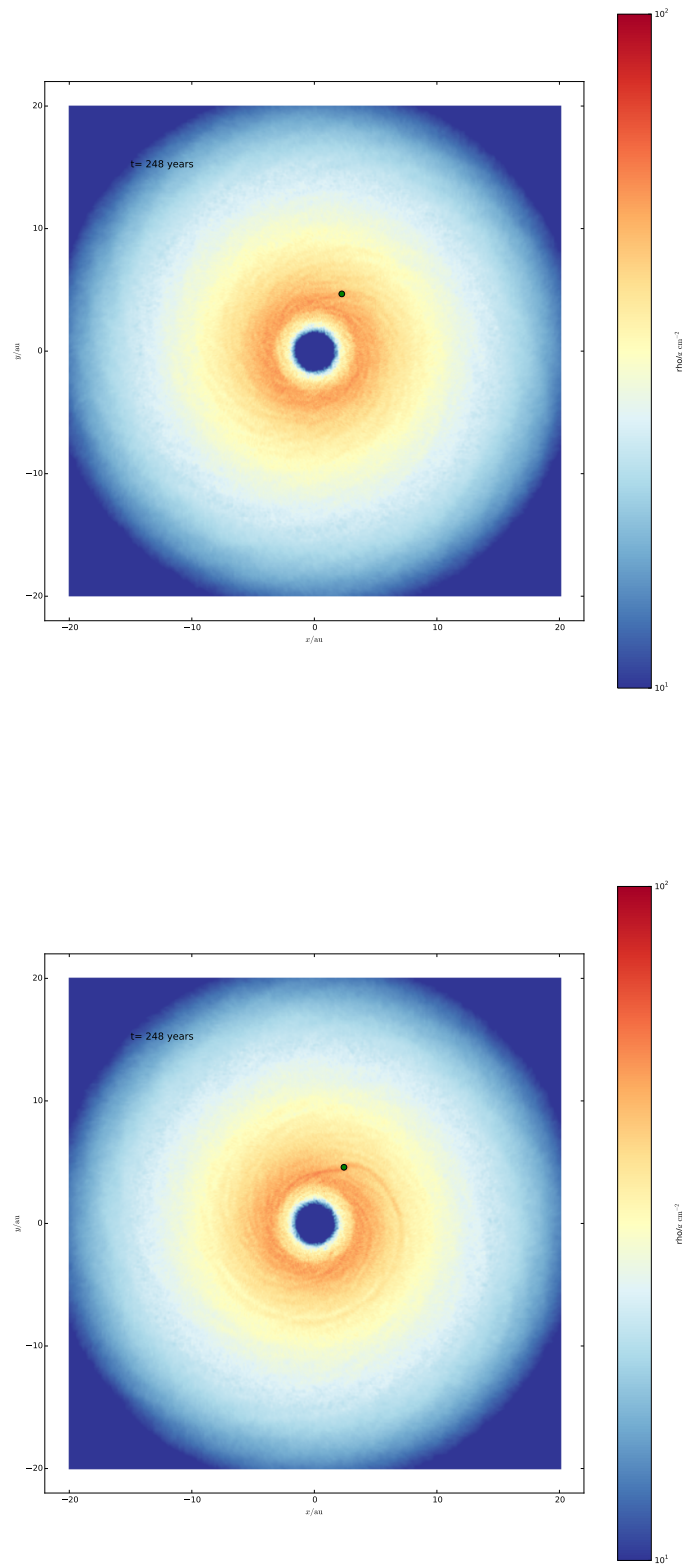


FIGURE 4.9: The 2D distribution of surface density of the light disk ( $0.005 M_{\odot}$ ) after planets  $10 M_{\oplus}$  (top) and  $33 M_{\oplus}$  (bottom) finish their growth.

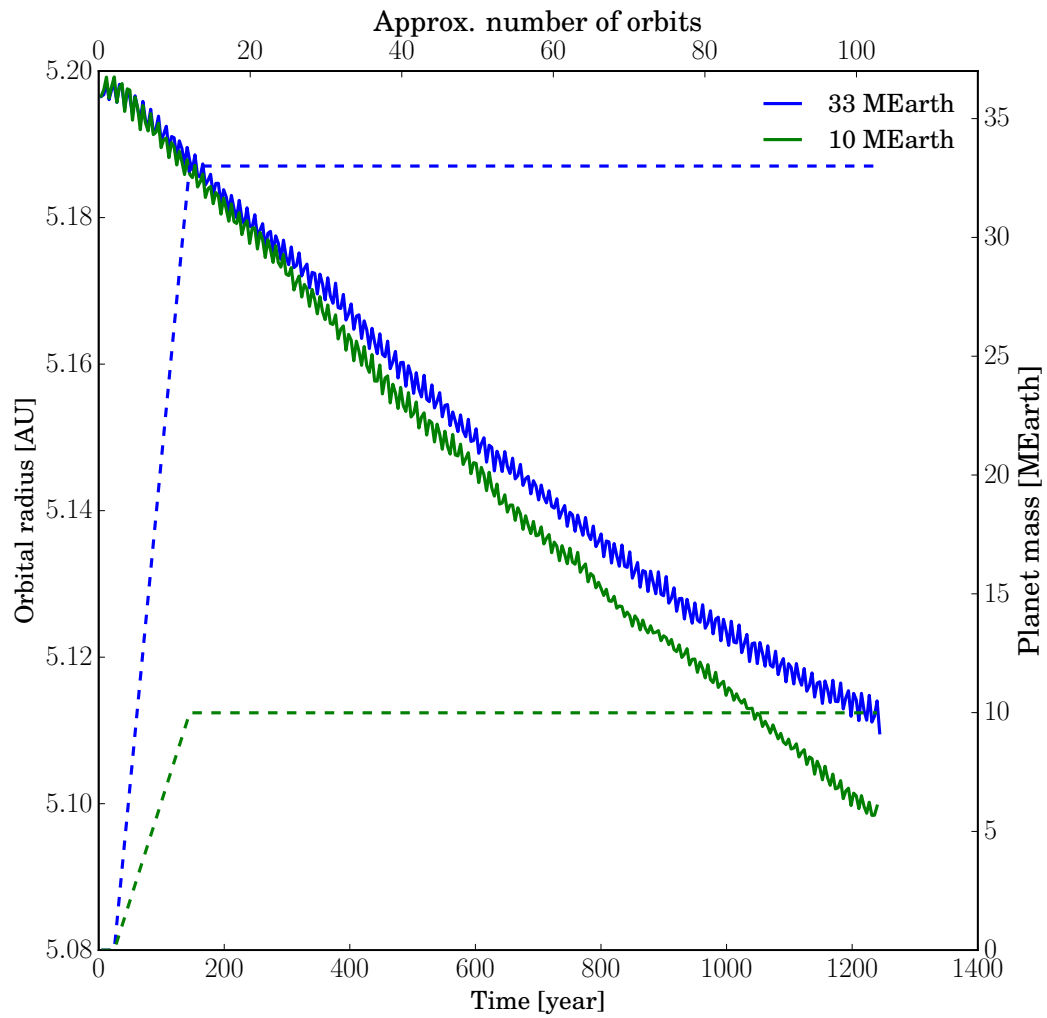


FIGURE 4.10: The orbital variation of two planets in protoplanetary disk of mass  $0.005 M_{\odot}$ . The dashed lines in matching colors indicate the growth in mass of the planets.

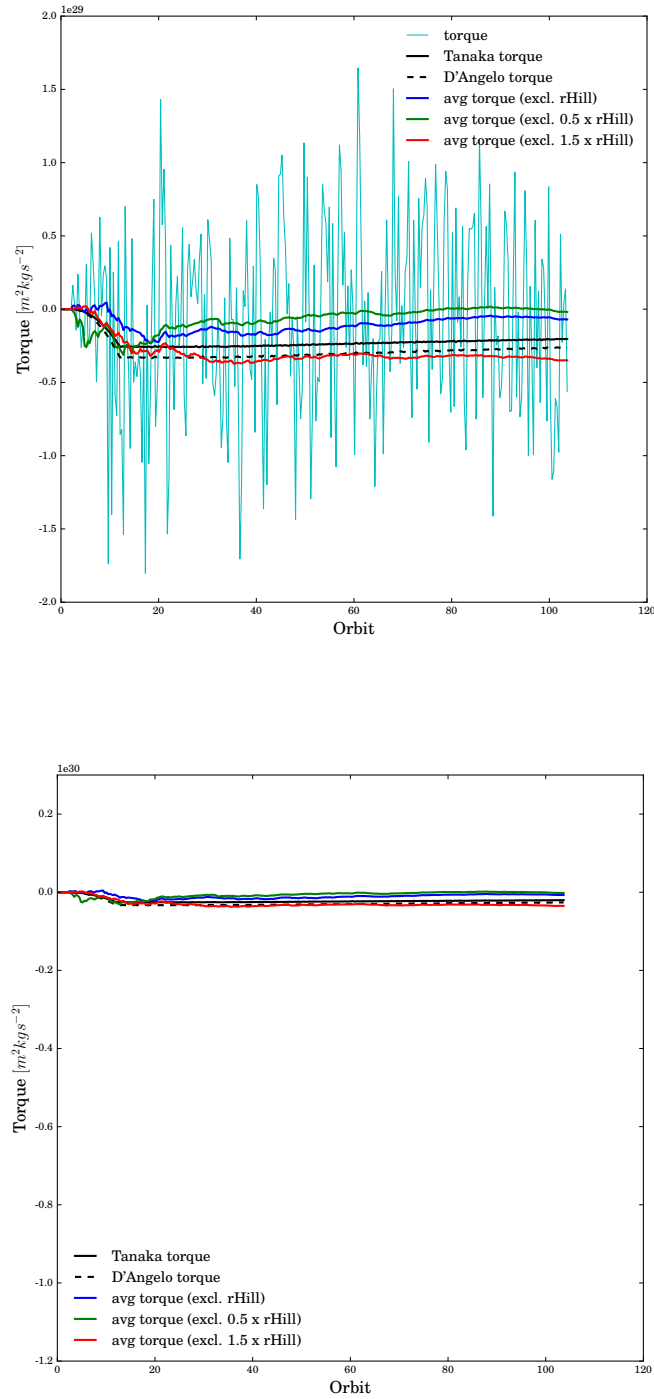


FIGURE 4.11: The evolution of the gas torque on  $10M_{\oplus}$  planet in  $0.005M_{\odot}$  disk. The linear estimation (black solid line) and numerical fitting (black dashed line) are taken from [Tanaka, Takeuchi & Ward \(2002\)](#) and [D'Angelo & Lubow \(2010\)](#), in comparison with averaged torque excluding the vicinity around planet (within 0.5, 1 and 1.5 Hill radius). The lower panel is for comparison at the same scale with [Fig. 4.12](#) and [4.22](#)

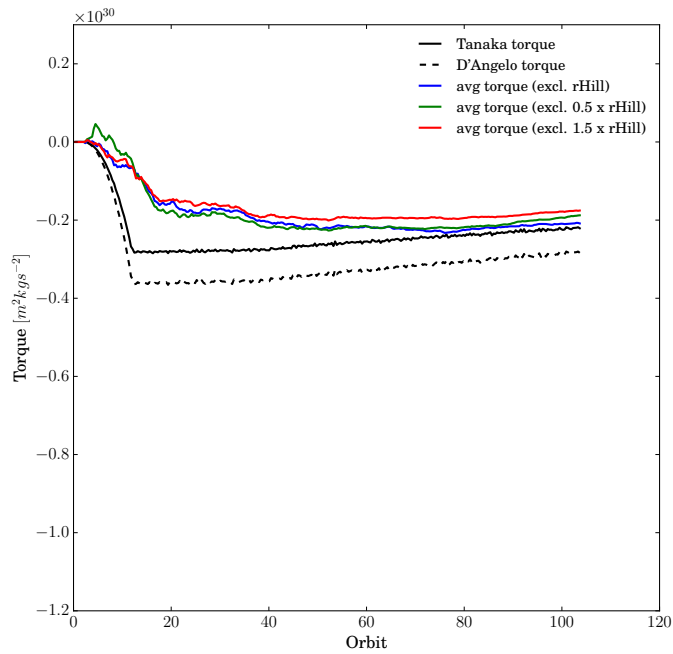
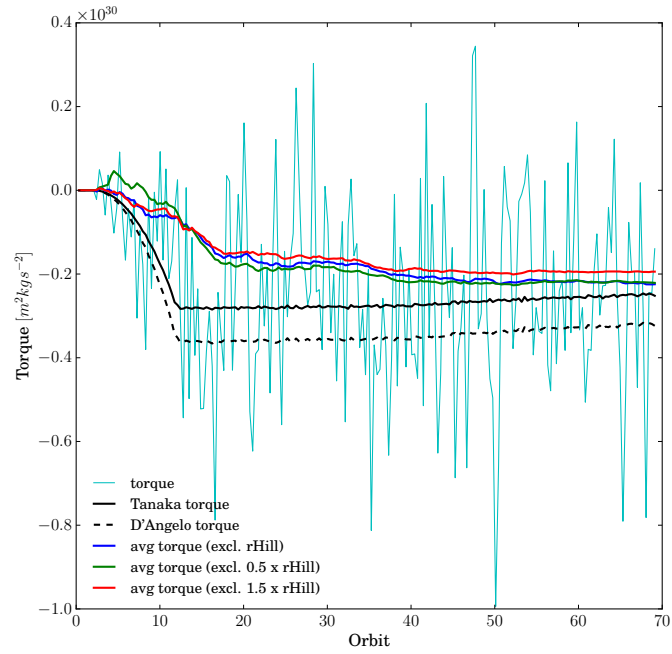


FIGURE 4.12: Same as Figure 4.11, but for  $33 M_{\oplus}$  planet in  $0.005 M_{\odot}$  disk.



same scale to allow for easy comparison between the two simulations.

Although the gas torque on planet (cyan thin line) is noisy (as seen previously for the borderline stable disks in Fig. 4.5) and flips the sign regularly, the averaged torque is always negative, suggesting the outer resonances dominate and favor an inward migration. For the first 20 orbits, the average torque steadily increases in magnitude before settling to a more steady value, reflecting the growth and settling of the planet in early stage. This period is the saturation of the co-rotational torque, which initially opposes the torque from the Lindblad resonances before the disk adjusts the angular momentum around that region as shown in Figure 2.2.

The linear analytical torque (black solid line) shown in Figure 4.12 is about 10 times larger than one in Figure 4.11, as predicted from Equation 2.9. This analytical torque decreases during the simulation, most markedly in Figure 4.12 for the heavier planet. Based on equation 2.9 and the disk profiles shown in Figure 4.8, this change is due to the local density at the planet position, which drops over the course of the simulation due to accretion onto the central star (Fig. 4.8). In equation 2.9, the torque is calculated from the local density assuming this local region remains on a power-law distribution. A lowered value therefore results in lowering both the inner and outer Lindblad estimates.

The averaged torque in both simulations agrees reasonably well with the idealised analytical estimate. Comparing with the semi-stable disks in Figure 4.5, this is clearly a case of a smooth migration where the Lindblad resonances appear to be controlling the motion. For this reason, it can be confirmed that the strong variations in the torque and planet motion in section 4.3 are due to the disk structure.

Despite this smooth migration and reasonable match of the calculated and analytical net torques, the actual migration of the planet does not closely follow the analytical prediction. Both planets move too swiftly through the disk, despite their net torques beyond 1 Hill radii suggesting a lower than predicted force on the planet. At approximately 1200 years, the linear analytical prediction for the location of the heavier  $33 M_{\oplus}$  planet is about 5.142 AU, while the  $10 M_{\oplus}$  planet should be at 5.175 AU.

There are a few possible reasons for this discrepancy. The first is that the planet's orbit is slightly eccentric and is being damped by the gas. This will also extract angular momentum from the planet's motion and result in an accelerated path towards the star. A second issue may also stem from the fall-off in disk density before the location of the inner Lindblad resonance (see Figure 4.8), which increases the negative differential torque favoring a fast inward migration. In the comparable simulation carried out by [Ayliffe & Bate \(2010\)](#), the results show an agreement with linear calculations because the authors measured only the last 25 orbits out of a total of 50 orbits, which may be short enough to prevent the collapse of the inner edge. A third issue may be one

of resolution, which may be preventing an accurate measurement of forces directly surrounding the planet. This will be considered in more detail in the section 4.2.2.

It is notable that [Ayliffe & Bate \(2010\)](#) focused on the comparison of the torques, not the planet progression. This is commonly done in planet migration research, feasibly because there is a more direct comparison in the torques beyond 1 Hill radii than in the motion of the planet where all forces will be at work. In simulations where the motion of the planet is plotted, similar issues with matching the orbital progression are reported ([Lufkin, et al., 2004](#)). It is also quite common to hold the planet in a fixed circular orbit and estimate the migration timescale by measuring the torques in this configuration ([Paardekooper & Mellema, 2006](#); [Bate, et al., 2003](#); [D'Angelo & Lubow, 2010](#)).

Taken together, it appears that while the torque on the planet agrees well with the theory for Type I migration, the actual planet movement is difficult to simulate accurately. For that reason, the timescale of the migration is difficult to use as a measure of influence of the disk's instability. Instead, our calculations will compare the torques in the relevant runs.

On the other hand, in case of lighter planet whose Roche sphere is smaller (Eq. 4.1), widening the exclusion region of vicinity around the planet from 0.5 Hill radii to 1.5 Hill radii results in an increase in the net torque value (in magnitude) (green and red lines in Fig. 4.11), which is opposing to case of massive planet (Fig. 4.12). This may suggest that the planet's motion is being disproportionately influenced by particles very close to its position. Such a situation could occur if the scale of the Hill radius is being poorly resolved within the simulation. This will be considered in section 4.2.2.

## 4.2.2 Resolution sensitivity of migration

To test the impact of resolution on our results, we ran the low-mass,  $10 M_{\oplus}$  planet in the light,  $0.005 M_{\odot}$ , disk described in section 4.2.1 at double the resolution with 2 million gas particles. Of the two runs in this previous section, the lower mass planet is expected to have the most dependence on resolution.

The low-mass planet drives only small perturbation in the light homogeneous disk, so the Lindblad waves are weaker. Moreover, the planet's Hill radius is smaller and more difficult to resolve. This could lead to the region close to the planet having a stronger influence on its motion than is physically expected. Evidence that this might be happening is seen in Figure 4.11. In the simulation with the heavier,  $33 M_{\oplus}$  planet, a decrease in the torque is seen as a larger region (from 0.5 Hill radii to 1.5 Hill radii) is excluded from the force calculation. However, for the  $10 M_{\oplus}$  planet, the trend is reversed, although the torques remain close in magnitude.

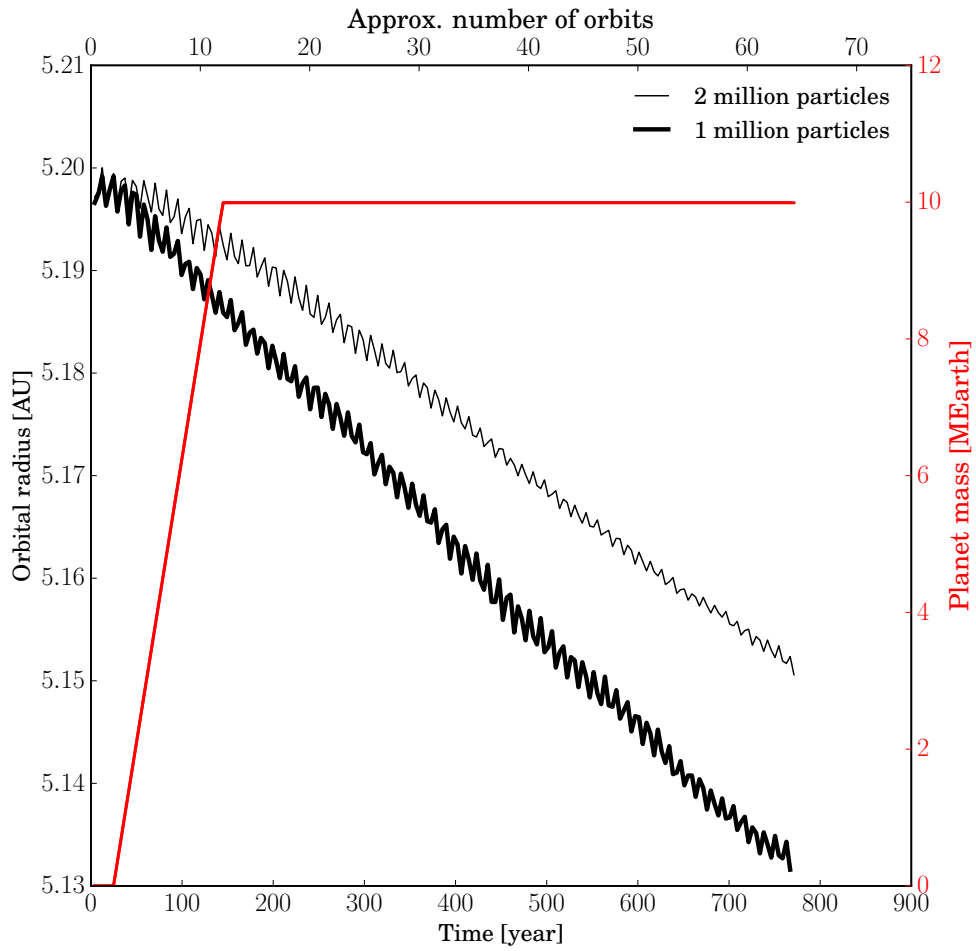


FIGURE 4.13: The orbital evolution of a  $10 M_{\oplus}$  planet in  $0.005 M_{\odot}$  disk resolved by two resolutions: 1 million (thick lower line) and 2 million (thin upper line) particles. The red line indicates the growth in mass of the planet.

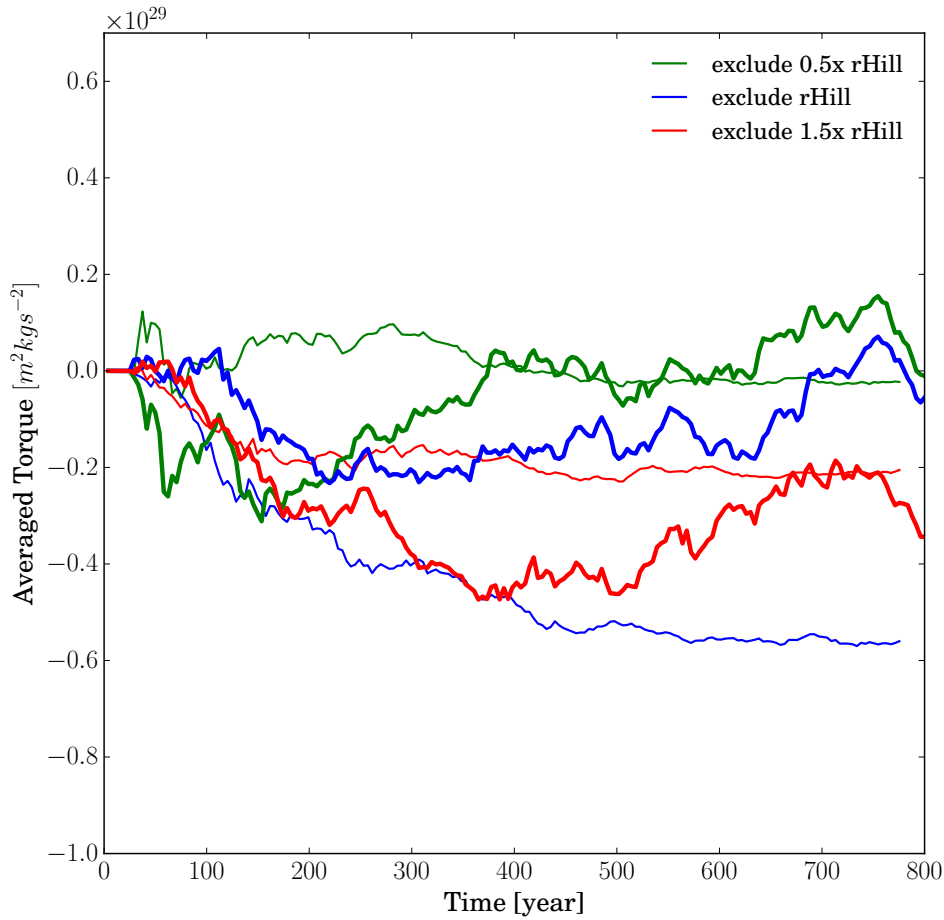


FIGURE 4.14: The evolution of averaged torque exerted on  $10M_{\oplus}$  planet by  $0.005M_{\odot}$  disk resolved by two resolutions: 1 million (thick lines) and 2 million (thin lines) particles.

A comparison to the original 1 million particle simulation and the 2 million particle simulation is presented in Figure 4.13, showing the distance from the planet to the star in which the lower thick line displays lower resolution while the thin upper line indicates higher one.

Although the resolution only increases double, the change of resultant migration rate seems notable. Planet in both simulations constantly moves inward but at slightly different rates. Higher resolution does show a smaller fluctuation of the orbital radius, suggesting more efficient gas damping. Overall, the migration rate is slowed, bringing it closer to the analytical expectation. Resolution is therefore a factor in why our light disk simulations in section 4.2 could not match results from [Ayliffe & Bate \(2010\)](#).

As mentioned in section 4.2, the inverse proportion between the averaged torque (absolute magnitude) and the exclusion radius shown in Fig. 4.11 is possibly a result from insufficiently high resolution. This is confirmed in Figure 4.14, showing the averaged torque exerted on  $10 M_{\oplus}$  planet resolved by two resolutions, 2 million particles presented by the thin lines and 1 million particles indicated by the thick lines. While the lower resolution shows an unexpected augmentation in torque values due to expansion of vicinity, the net torque excluding Hill radius in the high resolution run is larger than that excluding 1.5 Hill radii. This performance proves the sensitivity of the calculation on resolution. However, the smallest surrounding area, within 0.5 Hill radius around planet, is not well resolved at 2 million particles as the torque is still smallest rather than largest as expected.

Ideally, the simulation would be run at a sufficiently high resolution for the planet migration path to converge. However, this has proved prohibitive due to computational time. Shorter runs are insufficient for the torques to reach equilibrium and effect of disk structure to become apparent. Less runs would not permit a proper exploration of the parameter space. However the torques beyond a Hill radius appear to agree reasonably with the analytical prediction. We will therefore use these as the main quantitative measure.

## 4.3 Type I migration in borderline unstable disks

### 4.3.1 A massive planet in a heavy disk

Based on the discussion on the torque in the light disk above, simulations of a heavier disk were implemented to revisit the results from section 4.1. The main change from section 4.1 is that the protoplanetary disk is now very similar in profile shape and planet location to the light disks in section 4.2.1 so that direct comparison is possible.

The disk model is similar to that described in section 4.2 but its parameters are altered to create a disk on the brink of gravitational stability. To produce an instability of Toomre  $Q_{min} = 1$  and aim at a semi-stable disk, the disk mass and minimum temperature were chosen to be  $M_d = 0.07 M_{\odot}$ ,  $T_0 = 160 R^{-1}$  K. The disk mass seems to be far heavier than traditional MMSN by Hayashi (1981), but comparable to a new model erected by Desch (2007). As before, the  $33 M_{\oplus}$  planet was included once the disk had settled and raised from a gas-mass particle to its full mass over about 10 orbits.

The evolution of the disk parameters is shown in Figure 4.15. As the cooling process effectively diminishes the temperature down to the minimum profile before introducing the planet, the Toomre Q value does not alter over time and drops just below 1 at about 15 AU. However, near the planet location (interior 5.2 AU), the Toomre Q parameter is larger than this critical value. Similar to the light disk case (Section 4.2), the

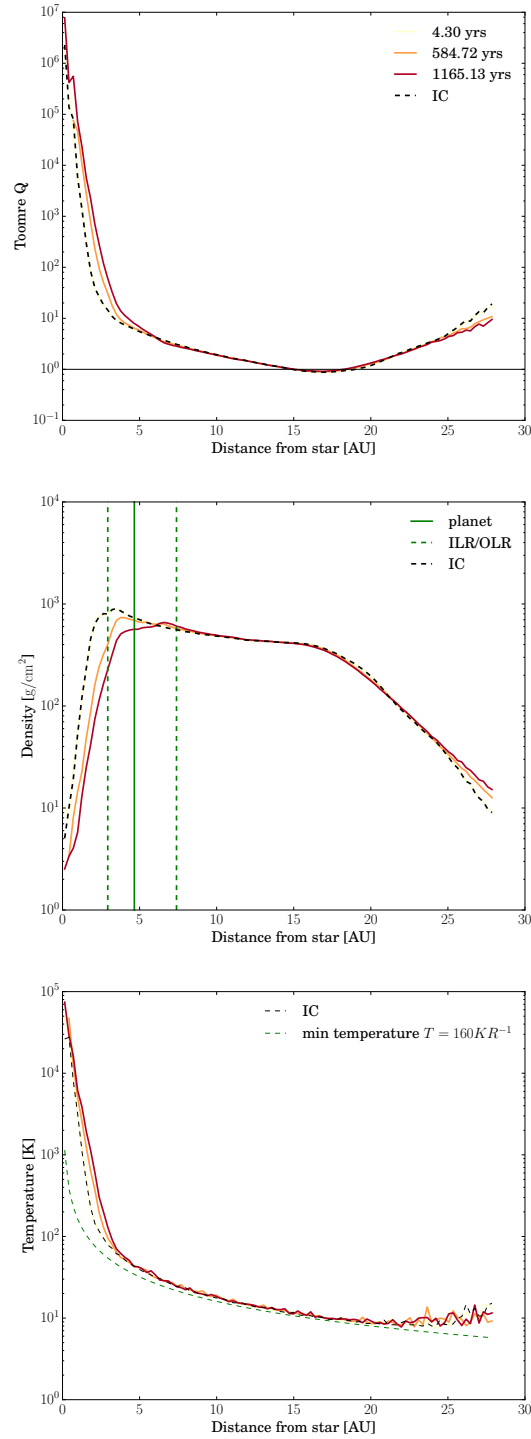


FIGURE 4.15: Top to bottom: Radial distribution of instability parameter, surface density and temperature of the massive disk ( $0.07M_{\odot}$ ). The black dashed lines indicate disk profiles before inserting planet. The horizontal line in top panel illustrated  $Q = 1$ . The vertical lines in middle panel indicate locations of the planet (solid) and the innermost/outermost Lindblad resonances (dashed left/right) at the last output, i.e. 1165 years. The green dashed curve in bottom panel denotes the minimum temperature.

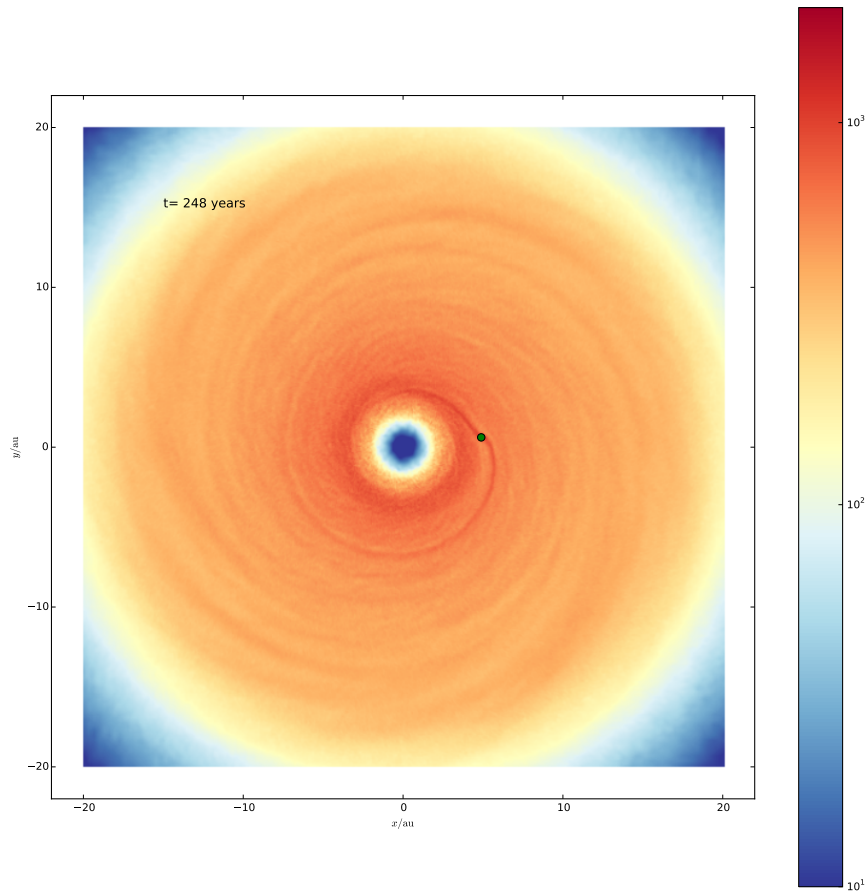


FIGURE 4.16: The 2D distribution of surface density of the massive disk ( $0.07 M_{\odot}$ ) after the planet (denoted by the green dot) finishes its growth.

inner Lindblad resonance by the end of the simulation also sits in the inner edge of the disk and suffers from a reduced density in this region.

As predicted from the property profiles in Figure 4.15, the image of the disk shown in the 2D distribution of surface density in Figure 4.16 contains notable structure compared to the comparative light disk in section 4.2.1, with denser flocculant spiral arms. The Lindblad resonances emanated by the planet (location indicated by the green dot) after its growth are able to be identified within the disk, implying significant influence on the disk gas.

Figure 4.17 presents the orbital evolution of a  $33 M_{\oplus}$  planet in the heavy disk along

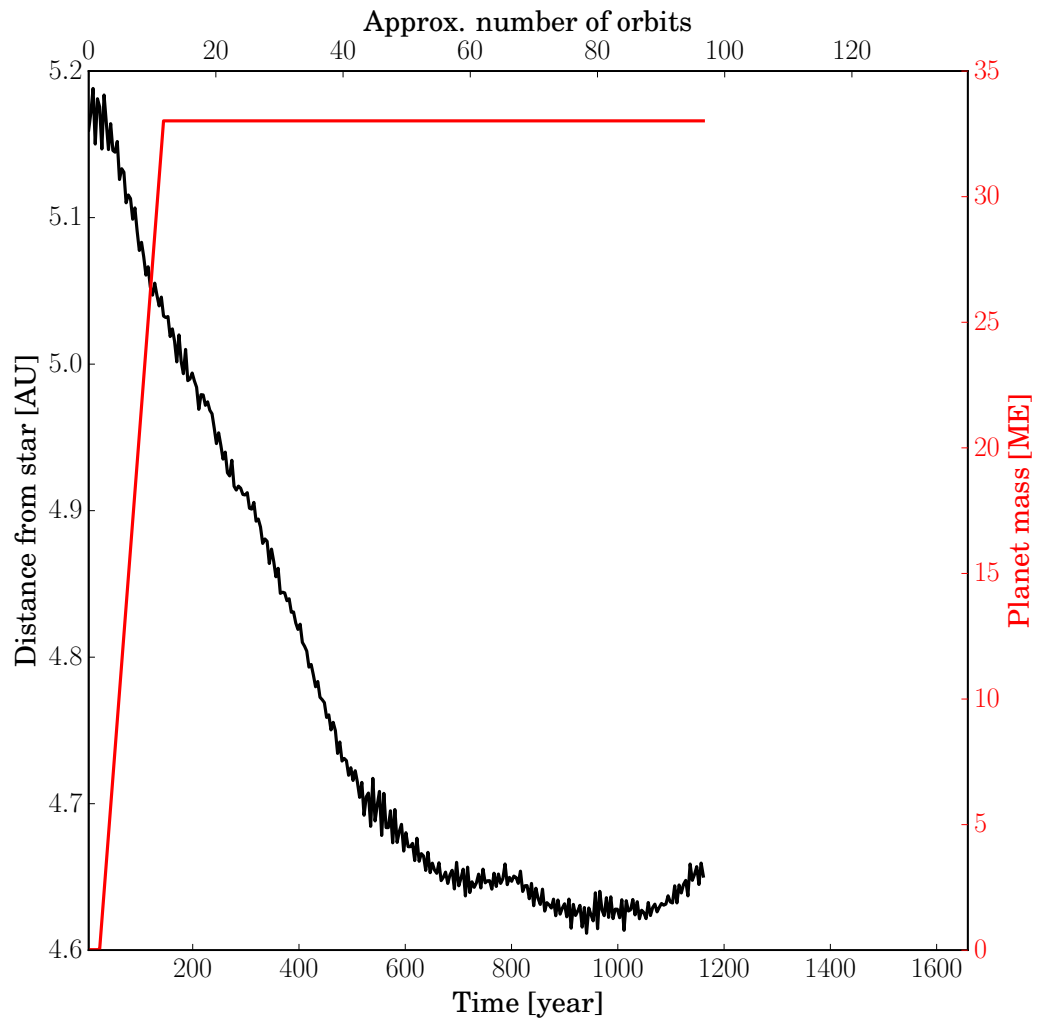


FIGURE 4.17: The variation of planet orbital radius in protoplanetary disk of mass  $0.07 M_{\odot}$  (black line). The red line indicates the increase in mass of the planet.



with its mass growth during the first 10 orbits. As a consequence of the strong interaction between the massive planet and the heavy disk, the elliptic orbits are more deformed compared to the same planet mass in the equivalent light disk in Figure 4.10. The planet rapidly drifts toward the star within around 20 orbits soon after it has finished growing. At around 40 orbits, however, the planet suddenly slows and seems to become trapped at the distance of 4.65 AU from the star. This manifestation likely indicates a transition from Type I to Type II migration.

Type II migration occurs when the planet can exchange sufficient angular momentum with the gas to create a gap in the protoplanetary disk. A gap can be maintained if the Hill radius of the planet exceeds the scale height of the disk, allowing the planet's gravity to push away (through the exchange of angular momentum) any gas that moves to fill the cavity. At this point, the planet's migration slows and becomes equal to the rate of viscous flow in the disk as this represents the rate gas will try and close the gap, and takes angular momentum from the planet.

The radial distribution of the surface density at later times does not indicate a notable hollow around the planet. On the other hand, the Hill radius of the planet (Eq. 4.1) is  $R_{\text{Hill}} = 0.15$  AU, comparable to the scale height of the disk,  $H = 0.16$  AU, indicating that the gap opening criteria is at least borderline fulfilled. The massive disk is also rich in structure and the density perturbations around the spiral may be sufficient to create a planet trap and minimize the torques as the planet begins to move to Type II migration.

The evolution of the torques on the planet are shown in Figure 4.18 with the same denotation as in Figure 4.11. The torque is not only much larger than in the light disk as predicted from analytical considerations, but also greatly departs from the linear analytical estimation for a larger mass disk. At the later half of the evolution, the torque tends to be positive, encouraging an outward migration at that point. This supports either the transition from Type I to Type II migration or a combination of the migration transition and planet trap driven by disk structure.

### 4.3.2 A low-mass planet in a heavy disk

To ensure the movement of the planet is pure Type I migration, we adopted a disk of mass  $M_d = 0.0875 M_{\odot}$  and temperature  $T = 250 \text{ K} R^{-1}$ , which has a scale height of about  $H = 0.2$  AU. With this disk, we embedded the lighter  $10 M_{\oplus}$  planet that has a Hill radius of  $R_{\text{Hill}} = 0.1$  AU at 5.2 AU.

According to Ward (1997) and Tanaka, Takeuchi & Ward (2002), the condition for applying the linear calculation for Type I migration is  $R_{\text{Hill}} \ll H$ , but Bate, et al. (2003) showed it is valid even if  $R_{\text{Hill}} \simeq 2H/3$ . Therefore, this planet should not be able to open a gap.

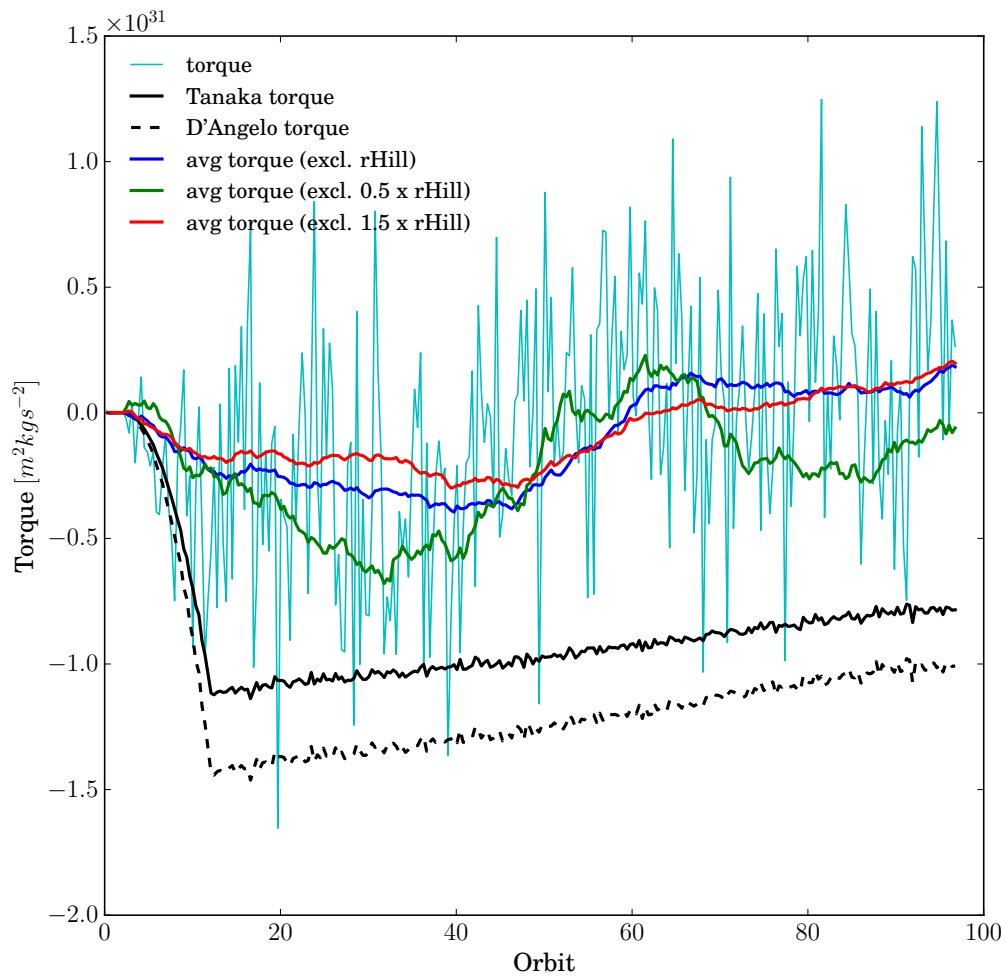


FIGURE 4.18: The evolution of the gas torque on  $33 M_{\oplus}$  planet in  $0.07 M_{\odot}$  disk. Same denotation as in Figure 4.11

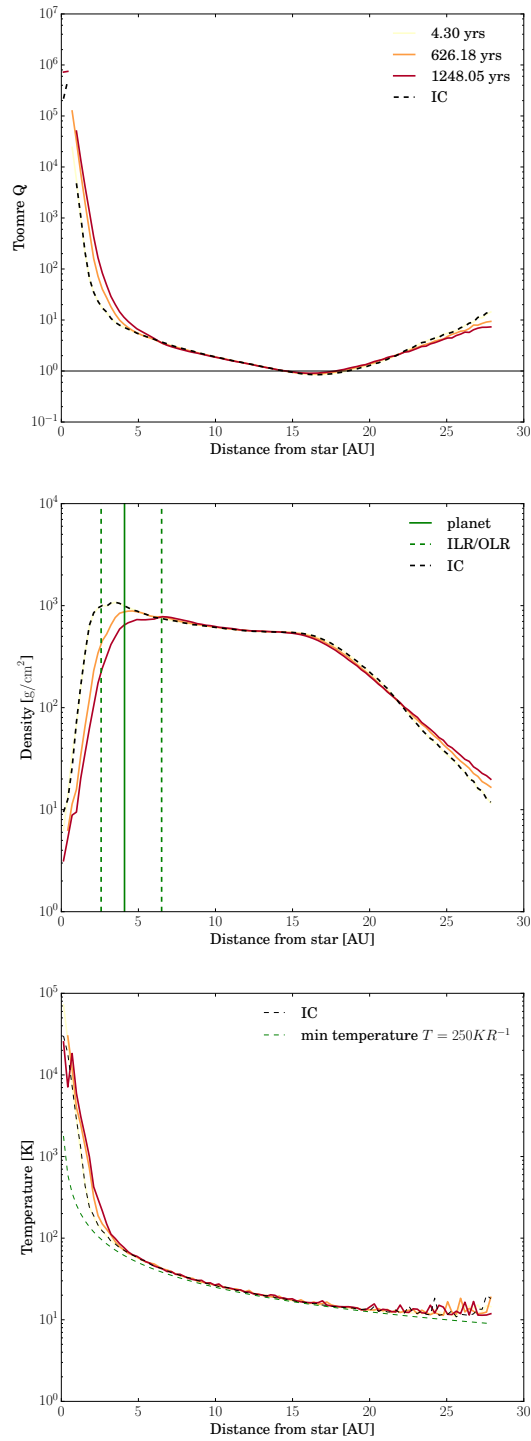


FIGURE 4.19: Same as Figure 4.15 for a  $10 M_{\oplus}$  planet in a massive disk of  $0.0875 M_{\odot}$ ,  $T = 250 \text{ K R}^{-1}$ .

This disk also drops below the instability threshold of  $Q \leq 1$  at large distances as illustrated in Figure 4.19. The properties of this disk model are extremely similar to the previous one in Section 4.3.1.

Owing to the almost identical Toomre  $Q$  profile to the disk in Section 4.3.1, the disk illustrates similar structure in 2D distribution of surface density shown in Figure 4.20, but appears to have slightly denser spiral arms. As the disk is a little more massive, the Lindblad waves excited by low-mass planet are nearly indistinguishable from the instability spirals, suggesting similar impacts on the planet.

The change in distance from the star during the evolution of a  $10 M_{\oplus}$  in this heaviest disk of  $0.0875 M_{\odot}$  is presented in Figure 4.21. The planet seed experiences a powerful interaction with the environment when initially inserted into the protoplanetary disk at 5.2 AU. This effect is seen more powerfully than in the lighter disk (Fig. 4.10) through the strong fluctuation of orbital radius at the very beginning of the planet's growth. Soon after adjusting to the gas disk and reaching its proper mass (first 20 orbits), the planet travels towards the star steadily, similarly to the planet in the light disk (Figure 4.10) but approximately 10 times faster (by eye). Nonetheless, the shape of the elliptical orbit is distorted, which also occurred to the  $33 M_{\oplus}$  in massive disk but not to the planet in light disk. This again demonstrates the influence of the heavy disk on the planet movement.

Sitting in the heavy cool disk, the planet is supposed to exchange more angular momentum with the surrounding gas than when embedded in a lighter or warmer disk. According to Eq. 2.9, compared to light warm disk (Section 4.2), the  $10 M_{\oplus}$  planet is expected to receive a 30 times larger torque from the gas to promote the migration. Figure 4.22 indicates how net torque changes during the journey of the planet. The black solid line presents the Tanaka, Takeuchi & Ward (2002) torque, and is 30 times larger than in Figure 4.11.

As we have seen in the previous massive disks, the torque on the planet is not steady, even though the migration rate is relatively smooth in this case. The lower panel of Figure 4.22 shows the torque on a matching scale with previous plots, and significant fluctuations in the torque can be seen, especially over the first 50 orbits.

## 4.4 Conclusion

In this thesis, we have shown that instabilities in a protoplanetary disk can have a strong impact on the torques and migration of a planet. When embedded in a smooth homogeneous disk, the planet has a slight, regular elliptical orbital motion and a steady migration rate. The measured torque on the planet settles after the saturation of the co-rotational torque and agrees well with linear analytical estimates for Type I

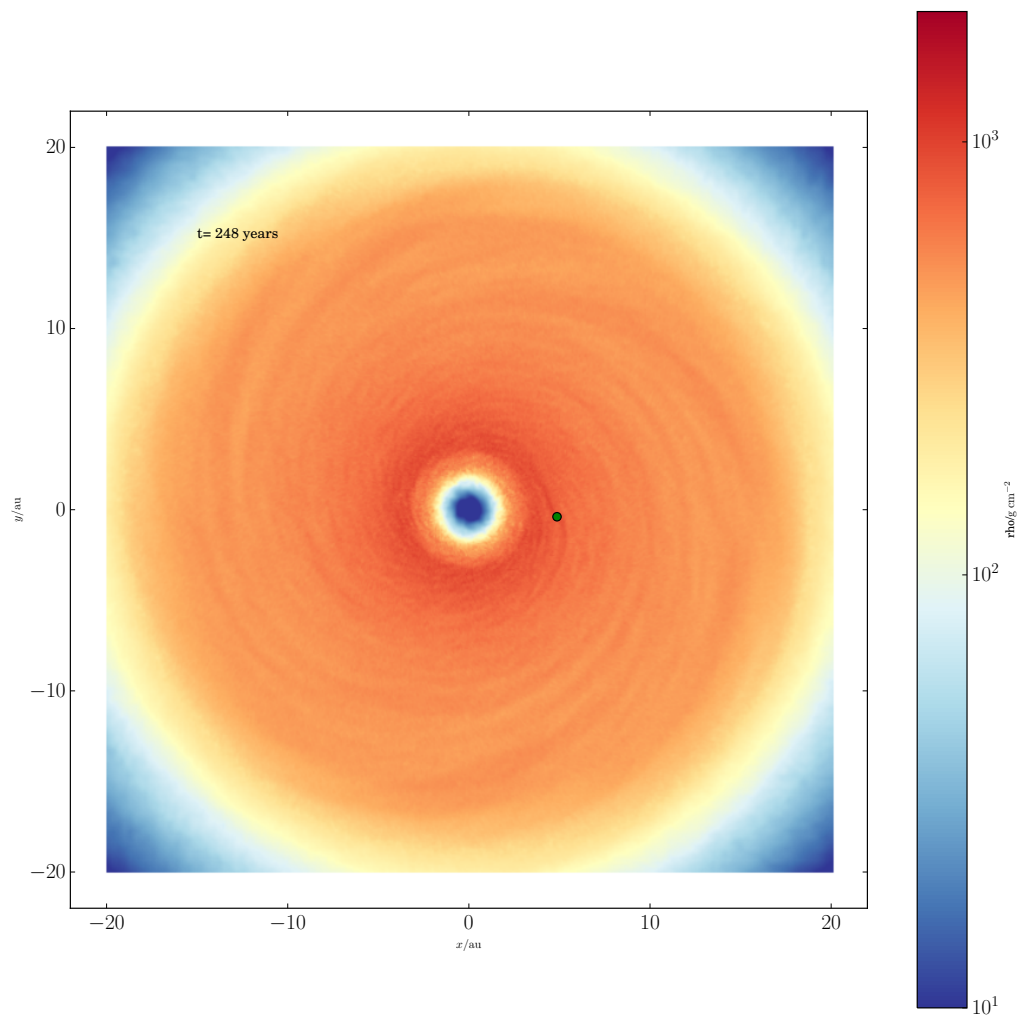


FIGURE 4.20: The 2D distribution of surface density of the massive disk ( $0.0875 M_{\odot}$ ) after  $10 M_{\oplus}$  planet finishes its growth.

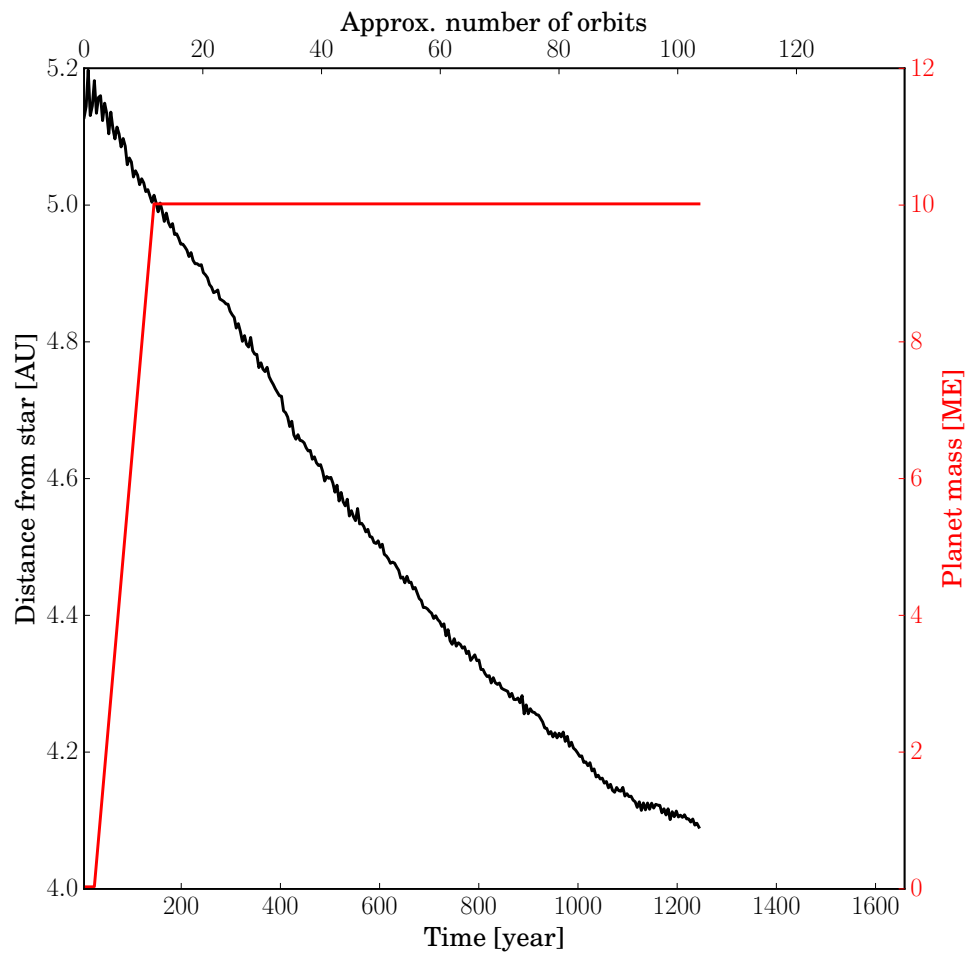


FIGURE 4.21: The variation of planet orbital radius in protoplanetary disk of mass  $0.0875 M_{\odot}$  (black line). The red line indicates the growth in mass of the planet.

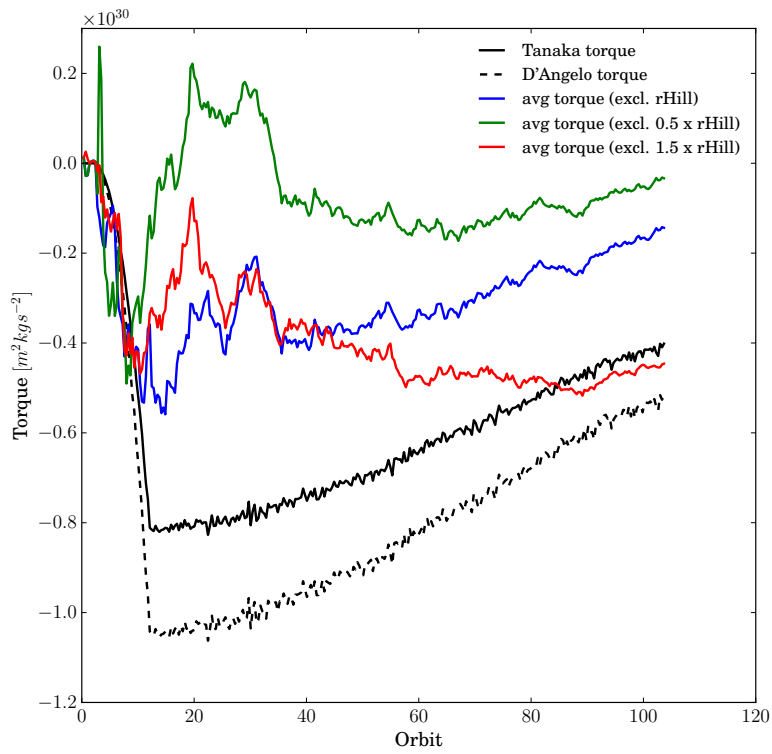
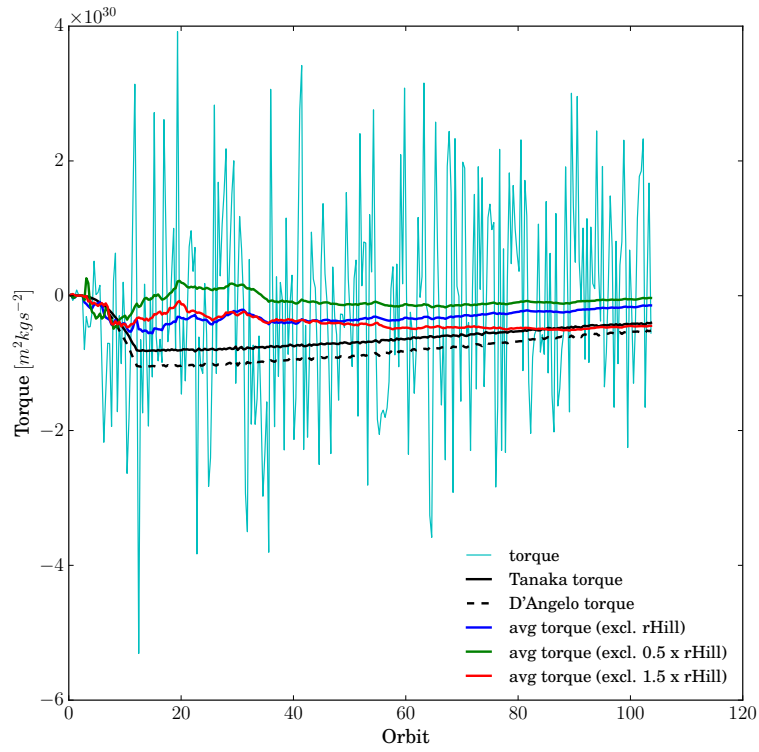


FIGURE 4.22: Same as Figure 4.11, but for  $10 M_{\oplus}$  planet in  $0.0875 M_{\odot}$  disk. The lower panel is in same scale as that in Figure 4.11, 4.12 for comparison.

migration. The largest impact on the planet's path and migration occurred for instability parameters that were between 1 - 2 (Figure 4.1 and 4.5). Despite higher values of  $Q$  at the planet position, the global environment rich in structure still had an impact on the planet's motion, distorting the elliptical orbit and potentially speeding up the migration rate (Figures 4.15, 4.17, 4.19, 4.21). The domination of the disk instabilities over the Lindblad torque does show large deviation from the analytical prediction and strong fluctuation in torque (Fig. 4.18, 4.22). This appears to be true regardless of planet mass. Lower value of  $Q$  in fragmenting disk results in gravitational scattering of the planet. There is evidence that disk instabilities close to the gap-opening stage for a planet may lead to planet traps and flip the direction of the torque on the planet (Figure 4.17).

Following the results from this thesis, future work will focus on planets in critically unstable disks to determine which is the most effective at disrupting planet migration.



# Bibliography

- Andrews S. M., Wilner D. J., Hughes A. M., Qi C., Dullemond C. P., 2009, *ApJ*, 700, 1502
- Andrews S. M., et al., 2018, *ApJL*, 869, L41
- Artymowicz P., 1993, *ApJ*, 419, 155
- Ayliffe B. A., Bate M. R., 2010, *MNRAS*, 408, 876
- Backus I., Quinn T., 2016, *MNRAS*, 463, 2480
- Baillié K., Charnoz S., Pantin E., 2016, *AA*, 590, A60
- Barnes J., Hut P., 1986, *Natur*, 324, 446
- Baruteau C., Masset F., 2008, *ApJ*, 678, 483
- Baruteau C., Masset F., 2008, *IAUS*, 397, IAUS..249
- Bate M. R., Lubow S. H., Ogilvie G. I., Miller K. A., 2003, *MNRAS*, 341, 213
- Beaugé C., Nesvorný D., 2012, *ApJ*, 751, 119
- Beckwith S. V. W., Sargent A. I., Chini R. S., Guesten R., 1990, *AJ*, 99, 924
- Bell K. R., Cassen P. M., Klahr H. H., Henning T., 1997, *ApJ*, 486, 372
- Benisty M., et al., 2015, *AA*, 578, L6
- Bitsch B., Kley W., 2011, *AA*, 536, A77
- Boss A. P., 1989, *PASP*, 101, 767
- Boehler Y., et al., 2018, *ApJ*, 853, 162
- Brummel-Smith C., et al., 2019, *JOSS*, 4, 1636
- Christiaens V., Casassus S., Perez S., van der Plas G., Ménard F., 2014, *ApJL*, 785, L12
- Daddi, E., Elbaz, D., Walter, F., et al. 2010, *ApJL*, 714, L118
- D'Angelo G., Kley W., Henning T., 2003, *ApJ*, 586, 540
- D'Angelo G., Lubow S. H., 2010, *ApJ*, 724, 730
- Davis S. S., 2005, *ApJL*, 627, L153

- Dib, S., Helou, G., Moore, T. J. T., Urquhart, J. S., & Dariush, A. 2012, *ApJ*, 758, 125
- Desch S. J., 2007, *ApJ*, 671, 878
- Dong R., Najita J. R., Brittain S., 2018, *ApJ*, 862, 103
- Fedele D., et al., 2017, *AA*, 600, A72
- Fedele D., et al., 2018, *AA*, 610, A24
- Gammie C. F., 2001, *ApJ*, 553, 174
- Goldreich P., Tremaine S., 1980, *ApJ*, 241, 425
- Guilet J., Baruteau C., Papaloizou J. C. B., 2013, *MNRAS*, 430, 1764
- Guilera O. M., Cuello N., Montesinos M., Miller Bertolami M. M., Ronco M. P., Cuadra J., Masset F. S., 2019, *MNRAS*, 486, 5690
- Hasegawa Y., Pudritz R. E., 2011, *MNRAS*, 417, 1236
- Hayashi C., 1981, *PThPS*, 70, 35
- Izumi, N., Kobayashi, N., Yasui, C., et al. 2014, *ApJ*, 795, 66
- Haworth T. J., Facchini S., Clarke C. J., Mohanty S., 2018, *MNRAS*, 475, 5460
- Jang-Condell H., Sasselov D. D., 2005, *ApJ*, 619, 1123
- Jiménez M. A., Masset F. S., 2017, *MNRAS*, 471, 4917
- Kenyon S. J., Hartmann L., 1995, *ApJS*, 101, 117
- Kennicutt, R. C., Jr. 1998, *ApJ*, 498, 541
- Kley W., Crida A., 2008, *AA*, 487, L9
- Kley W., Bitsch B., Klahr H., 2009, *AA*, 506, 971
- Kley W., Nelson R. P., 2012, *ARAA*, 50, 211
- Koda, J., Scoville, N., Sawada, T., et al. 2009, *ApJL*, 700, L132
- Lega E., Crida A., Bitsch B., Morbidelli A., 2014, *MNRAS*, 440, 683
- Lega E., Morbidelli A., Bitsch B., Crida A., Szulágyi J., 2015, *MNRAS*, 452, 1717
- Lufkin, G., Quinn, T., Wadsley, J., Stadel, J., Governato, F., 2004, *MNRAS*, 347, 421
- Lyra W., Paardekooper S.-J., Mac Low M.-M., 2010, *ApJL*, 715, L68
- Masset F. S., Casoli J., 2010, *ApJ*, 723, 1393
- Mayor M., Queloz D., 1995, *Natur*, 378, 355

- Meidt, S., Schinnerer, E., Garcia-Burillo, S., et al. 2012, American Astronomical Society Meeting Abstracts #219, 219, 346.16
- Menon H., Wesolowski L., Zheng G., Jetley P., Kale L., Quinn T., Governato F., 2015, ComAC, 2, 1
- Menou K., Goodman J., 2004, ApJ, 606, 520
- Meru F., Bate M. R., 2011, MNRAS, 410, 559
- Meru F., Bate M. R., 2012, MNRAS, 427, 2022
- Morales J. C., et al., 2019, Sci, 365, 1441
- Nelson A. F., Benz W., 2003, ApJ, 589, 556
- Nelson A. F., Benz W., 2003, ApJ, 589, 578
- Nelson R. P., Papaloizou J. C. B., 2004, MNRAS, 350, 849
- Nelson R. P., 2018, haex.book, 139, haex.book
- Nguyen N. K., Pettitt A. R., Tasker E. J., Okamoto T., 2018, MNRAS, 475, 27
- Paardekooper S.-J., Mellema G., 2006, AA, 459, L17
- Paardekooper S.-J., Mellema G., 2008, AA, 478, 245
- Paardekooper S.-J., Papaloizou J. C. B., 2009, MNRAS, 394, 2283
- Paardekooper S.-J., Baruteau C., Crida A., Kley W., 2010, MNRAS, 401, 1950
- Paardekooper S.-J., Baruteau C., Kley W., 2011, MNRAS, 410, 293
- Papaloizou J. C. B., Nelson R. P., Kley W., Masset F. S., Artymowicz P., 2007, prpl.conf, 655, prpl.conf
- Pérez L. M., et al., 2016, Sci, 353, 1519
- Rice W. K. M., Armitage P. J., Bonnell I. A., Bate M. R., 2003, ESASP, 539, 555, ESASP.539
- Rice W. K. M., Lodato G., Armitage P. J., 2005, MNRAS, 364, L56
- Rogers P. D., Wadsley J., 2012, MNRAS, 423, 1896
- Roman-Duval, J., Jackson, J. M., Heyer, M., Rathborne, J., & Simon, R. 2010, ApJ, 723, 492
- Schmidt, M. 1959, ApJ, 129, 243
- Shakura N. I., Sunyaev R. A., 1973, AA, 500, 33
- Stolker T., et al., 2016, AA, 595, A113
- Sun, Y., Su, Y., Zhang, S.-B., et al. 2017, ApJS, 230, 17

Tanaka H., Takeuchi T., Ward W. R., 2002, *ApJ*, 565, 1257

Toomre, A. 1964, *ApJ*, 139, 1217

Ward W. R., 1997, *Icar*, 126, 261

Wadsley J. W., Stadel J., Quinn T., 2004, *NewA*, 9, 137